

Early observations of the nearby type Ia supernova SN 2015F

R. Cartier¹★, M. Sullivan¹, R. Firth¹, G. Pignata^{2,3}, P. Mazzali^{4,5}, K. Maguire⁶,
M. J. Childress¹, I. Arcavi^{7,8}, C. Ashall⁴, B. Bassett^{9,10,11}, S. M. Crawford⁹, C. Frohmaier¹,
L. Galbany^{12,13}, A. Gal-Yam¹⁴, G. Hosseinzadeh^{7,8}, D. A. Howell^{7,8}, C. Inserra⁶, J. Johansson¹⁴,
E. K. Kasai^{9,10,11,15}, C. McCully^{7,8}, S. Prajs¹, S. Prentice⁴, S. Schulze^{3,16}, S. J. Smartt⁶,
K. W. Smith⁶, M. Smith¹, S. Valenti^{7,8}, and D. R. Young⁶

¹Department of Physics and Astronomy, University of Southampton, Southampton, Hampshire, SO17 1BJ, UK

²Departamento de Ciencias Físicas, Universidad Andres Bello, Avda. Republica 252, Santiago, Chile

³Millennium Institute of Astrophysics, Santiago, Chile

⁴Astrophysics Research Institute, Liverpool John Moores University, IC2, Liverpool Science Park, 146 Brownlow Hill, Liverpool L3 5RF, UK

⁵Max-Planck-Institut für Astrophysik, Karl-Schwarzschild-Str. 1, D-85748 Garching, Germany

⁶Astrophysics Research Centre, School of Mathematics and Physics, Queens University Belfast, Belfast BT7 1NN, UK

⁷Las Cumbres Observatory Global Telescope Network, 6740 Cortona Dr., Suite 102 Goleta, Ca 93117

⁸Department of Physics, University of California, Santa Barbara, CA 93106-9530, USA

⁹South African Astronomical Observatory, P.O.Box 9, Observatory 7935, South Africa

¹⁰African Institute for Mathematical Sciences, 6-8 Melrose Road, Muizenberg 7945, South Africa

¹¹Department of Mathematics and Applied Mathematics, University of Cape Town, Rondebosch, 7700, South Africa

¹²Pittsburgh Particle Physics, Astrophysics, and Cosmology Center (PITT PACC).

¹³Physics and Astronomy Department, University of Pittsburgh, Pittsburgh, PA 15260, USA.

¹⁴Department of Particle Physics and Astrophysics, Weizmann Institute of Science, Rehovot 76100, Israel

¹⁵Department of Physics, University of Namibia, 340 Mandume Ndemufayo Avenue, Pioneerspark, Windhoek, Namibia

¹⁶Instituto de Astrofísica, Facultad de Física, Pontificia Universidad Católica de Chile, Vicuña Mackena 4860, 7820436 Macul, Santiago, Chile

Accepted 2016 October 14. Received 2016 October 11; in original form 2016 May 25

ABSTRACT

We present photometry and time-series spectroscopy of the nearby type Ia supernova (SN Ia) SN 2015F over -16 days to $+80$ days relative to maximum light, obtained as part of the Public ESO Spectroscopic Survey of Transient Objects (PESSTO). SN 2015F is a slightly sub-luminous SN Ia with a decline rate of $\Delta m_{15}(B) = 1.35 \pm 0.03$ mag, placing it in the region between normal and SN 1991bg-like events. Our densely-sampled photometric data place tight constraints on the epoch of first light and form of the early-time light curve. The spectra exhibit photospheric C II $\lambda 6580$ absorption until -4 days, and high-velocity Ca II is particularly strong at < -10 days at expansion velocities of ≈ 23000 km s⁻¹. At early times, our spectral modelling with SYN++ shows strong evidence for iron-peak elements (Fe II, Cr II, Ti II, and V II) expanding at velocities > 14000 km s⁻¹, suggesting mixing in the outermost layers of the SN ejecta. Although unusual in SN Ia spectra, including V II in the modelling significantly improves the spectral fits. Intriguingly, we detect an absorption feature at ~ 6800 Å that persists until maximum light. Our favoured explanation for this line is photospheric Al II, which has never been claimed before in SNe Ia, although detached high-velocity C II material could also be responsible. In both cases the absorbing material seems to be confined to a relatively narrow region in velocity space. The nucleosynthesis of detectable amounts of Al II would argue against a low-metallicity white dwarf progenitor. We also show that this 6800 Å feature is weakly present in other normal SN Ia events, and common in the SN 1991bg-like sub-class.

Key words: supernovae: general – supernovae: individual (SN 2015F)

1 INTRODUCTION

The uniformity of type Ia supernova (SN Ia) light curves allows them to be used as reliable distance indicators, providing crucial

★ E-mail: r.cartier-ugarte@soton.ac.uk (RC)

evidence for the accelerated expansion of the universe (Riess et al. 1998; Perlmutter et al. 1999). Despite many years of research and the general agreement that the progenitor stars of SNe Ia are accreting carbon-oxygen (CO) white dwarfs in binary systems, the nature of the companion star (Maoz et al. 2014), and the detailed physics of the explosion, remain uncertain.

The study of the outer layers of SN Ia ejecta can, in principle, provide important clues about the progenitor white dwarf and explosion physics by tracing the extent and amount of any unburnt material and the metallicity of the progenitor star (Höflich et al. 1998; Lentz et al. 2000; Walker et al. 2012; Maguire et al. 2012; Foley 2013; Mazzali et al. 2014). In particular, early ultraviolet (UV) spectra are sensitive to the abundance of iron-group elements in the outermost layers, and can place important constraints on progenitor metallicity (Hachinger et al. 2013; Maguire et al. 2012; Foley 2013; Mazzali et al. 2014). Any carbon detected in the outermost layers is particularly important, as carbon is the only element that could not be the result of thermonuclear burning, and can be directly associated with the original composition of the CO white dwarf. The amount and distribution of carbon can place strong constraints on the extension of the burning front and the degree of mixing during the explosion (Branch et al. 2003; Thomas et al. 2007; Parrent et al. 2012).

These outer layers can only be studied with early spectroscopic observations. The unburned material can be detected as absorption lines of C II in the optical (Parrent et al. 2011; Thomas et al. 2011a; Folatelli et al. 2012; Silverman & Filippenko 2012; Maguire et al. 2014; Cartier et al. 2014), and of C I in the near-infrared (NIR; Höflich et al. 2002; Marion et al. 2006, 2009; Hsiao et al. 2013, 2015; Marion et al. 2015). Recent studies have shown that at least 30 per cent of SNe Ia possess C II absorption lines prior to maximum light (Thomas et al. 2011a; Folatelli et al. 2012; Silverman & Filippenko 2012; Maguire et al. 2014).

Early spectra of SNe Ia also commonly exhibit ‘high-velocity’ (HV) features. These spectroscopic features correspond to absorption lines with expansion velocities much higher than the photospheric velocity, and usually greater than 15000 km s^{-1} , sometimes reaching 30000 km s^{-1} or higher at the earliest phases. The most common HV features are of Ca II, which seem to be a ubiquitous phenomenon at early stages (Mazzali et al. 2005; Childress et al. 2014b; Maguire et al. 2014; Silverman et al. 2015). HV features of Si II are rarer (see Marion et al. 2013; Childress et al. 2013; Silverman et al. 2015), and HV features of other ions (S II, Fe II, C II, O I) have also been claimed (Fisher et al. 1997; Hatano et al. 1999; Mazzali 2001; Branch et al. 2003; Garavini et al. 2004; Nugent et al. 2011; Marion et al. 2013; Cartier et al. 2014).

Such high expansion velocities suggest that HV features are produced in the outermost layers of the SN ejecta. Therefore, it is reasonable to hypothesize that their origin is tightly linked to the progenitor system and/or the physics of the burning in the outermost layers of the white dwarf. HV features are ubiquitous in SN Ia spectra at about a week prior to maximum light (Mazzali et al. 2005; Marion et al. 2013; Childress et al. 2014b; Maguire et al. 2014; Silverman et al. 2015; Zhao et al. 2015), and decrease in strength with time (Maguire et al. 2014; Silverman et al. 2015; Zhao et al. 2015). Possible explanations for HV features include density enhancements from swept-up (Gerardy et al. 2004) or distant (Tanaka et al. 2006) circumstellar material, abundance enhancements in the outermost layers of the ejecta (Mazzali et al. 2005), or variations of the ionization state in the outer layers due to non ‘local thermodynamic equilibrium’ (LTE) effects (Blondin et al. 2013). Their origin remains a puzzle.

The advent of high-cadence wide-area sky surveys over the last ten years has meant that the quality and quantity of early SN discoveries has increased, and with it has come a wealth of early SN Ia spectroscopy. In this paper, we present spectroscopy and photometry of the nearby SN Ia SN 2015F. In Section 2, we introduce SN 2015F and describe the photometry and spectroscopy, beginning at -16.30 d relative to peak brightness and extending to $+75.5 \text{ d}$ past peak. We also estimate the distance to the host of SN 2015F (NGC 2442), the rise time, and the epoch of first light. In Section 3, we analyse the spectroscopic data, and in Section 4 we model the spectra using the `syn++` code. We discuss our results in Section 5, and summarize in Section 6. Throughout, we assume a value for the Hubble constant of $H_0 = 70 \text{ km s}^{-1} \text{ Mpc}^{-1}$.

2 OBSERVATIONS

SN 2015F is located $43'.4$ north and $86'.2$ west of the centre of the nearby spiral galaxy NGC 2442, on the northern arm of NGC 2442, and was discovered on 2015 March 09.789 (all dates are UT) by Monard (2015) at $\alpha = 07^{\text{h}}36^{\text{m}}15^{\text{s}}.76$, $\delta = -69^{\circ}30'23''.0$ (see Fig. 1). The unfiltered discovery magnitude was 16.8. SN 2015F was promptly classified as a young SN Ia by the Public ESO Spectroscopic Survey of Transient Objects (PESSTO) collaboration on March 11.00 (Fraser et al. 2015). NGC 2442 is a SBbc galaxy with a recession velocity of $1466 \pm 5 \text{ km s}^{-1}$ in HyperLeda¹, and the Milky Way reddening along the line-of-sight to SN 2015F is $E(B - V)_{\text{MW}} = 0.175 \text{ mag}$ (Schlafly & Finkbeiner 2011), corresponding to a V -band extinction (A_V) of $\approx 0.54 \text{ mag}$.

The classification of SN 2015F as a young SN sparked a detailed spectroscopic and photometric follow-up campaign, which we detail in this section.

2.1 Photometry

We used several instruments to obtain photometry of SN 2015F, the main characteristics of which are summarized in Table 1. Data obtained with the European Southern Observatory (ESO) Faint Object Spectrograph and Camera (v2) (EFOSC2) on the New Technology Telescope (NTT) were reduced with the PESSTO pipeline described in detail in Smartt et al. (2015), and the Las Cumbres Observatory Global Telescope Network (LCOGT) images were reduced using the Observatory Reduction and Acquisition Control Data Reduction pipeline (ORAC-DR Jenness & Economou 2015). The reduction steps of the data obtained with the PROMPT telescopes are described in Pignata et al. (2011).

A optical photometric sequence of stars around the SN was calibrated in the UBV and gri bandpasses against standard stars from the Landolt (1992) and Smith et al. (2002) catalogues, respectively. The magnitudes of the optical photometric sequence around SN 2015F (see Fig. 1) are presented in Table A1 in the Appendix. Point spread function (PSF) fitting photometry was performed on the SN frames using DAOPHOT (Stetson 1987), and calibrated using the photometric sequence around the SN. The optical photometry of SN 2015F is in Table A2.

The NIR data were obtained with the Son of Isaac (SofI) camera on the NTT, and were reduced using our own IRAF² scripts

¹ <http://leda.univ-lyon1.fr/>

² IRAF is distributed by the National Optical Astronomy Observatory, which is operated by the Association of Universities for Research in Astron-

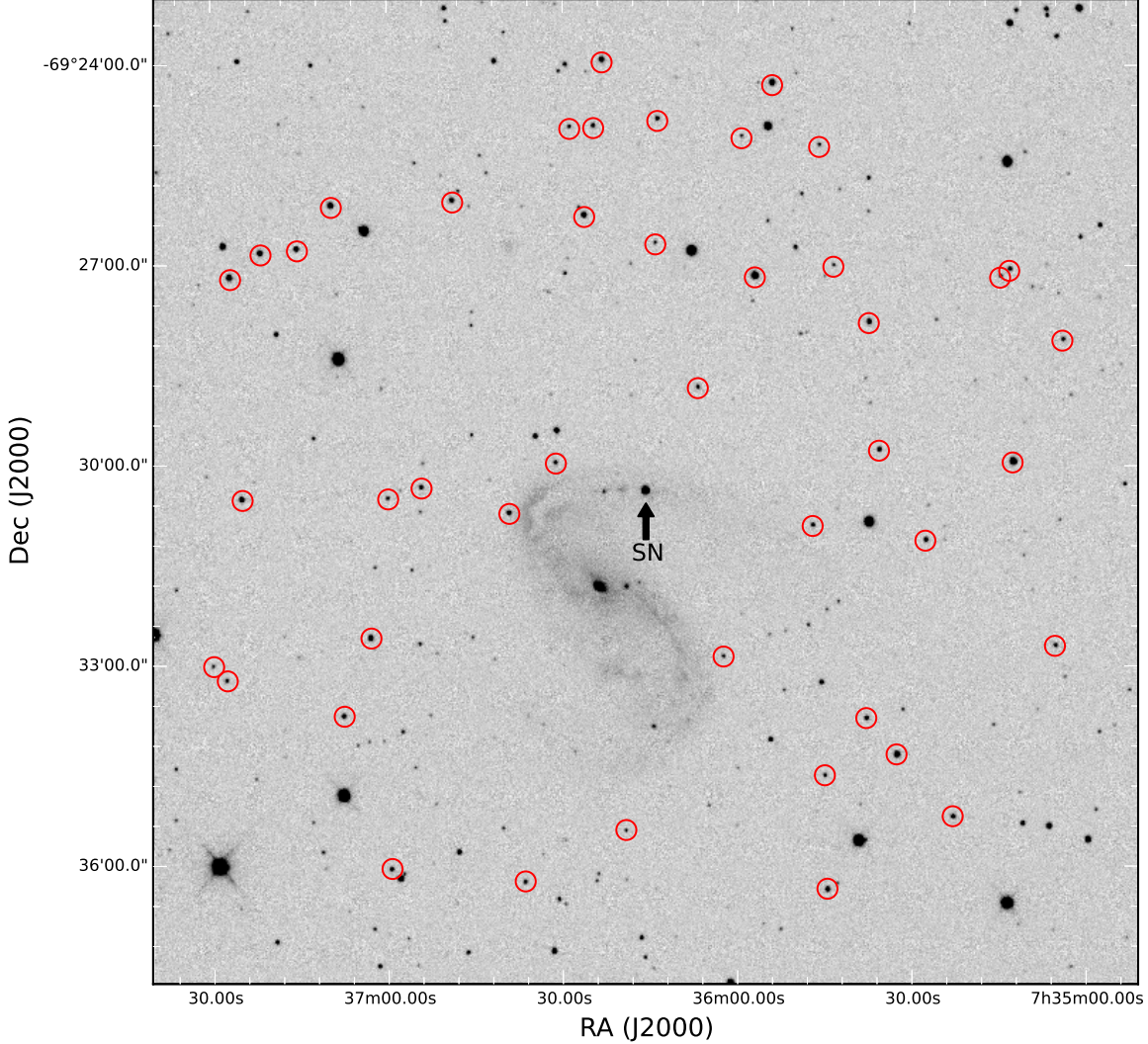


Figure 1. V-band image of the field of SN2015F obtained with the LCOGT 1-m telescope at the Siding Spring Observatory, Australia. The SN position is highlighted with an arrow. The stars of the photometric sequence around the SN, which were used to obtain differential photometry of the SN, are indicated with a red circle.

to create a clean sky image, which we subtract from the science images. Pixel-to-pixel variations were removed by dividing the science images by a flat field image. We used *SCAMP* (Bertin 2006) to obtain an astrometric solution, and *SWARP* (Bertin et al. 2002) to combine the dithered images into a single image. The NIR photometric sequence was calibrated by observing Persson et al. (1998) standard fields close in time and in airmass to the SN observations. The photometry of the NIR photometric sequence and of SN2015F are presented in Tables A3 and A4, respectively.

The *UBV*, *gri* and *JHK_s* light curves of SN2015F are shown in Fig. 2. Fitting a polynomial to the *B*-band light curve of SN2015F, we measure a decline rate of $\Delta m_{15}(B) = 1.35 \pm 0.03$ mag, and we estimate the epoch of maximum light as MJD 57106.45 ± 0.02 d (2015 March 25.4). Using the SiFTO light curve fitter (Conley et al. 2008), we determine a stretch of $s = 0.906 \pm 0.005$. A summary of the epoch of peak brightness, the peak magnitude, and the decline rate of the light curve (Δm_{15}) obtained from fitting a polynomial to the light curves of SN2015F in each filter is presented in Table 2.

In Table 3 we summarize the values of the host galaxy reddening along the line-of-sight to SN2015F ($E(B - V)_{\text{host}}$), calculated from the optical colours (Phillips et al. 1999), and *V*–NIR colours

Table 1. Summary of imagers used to observe SN 2015F.

Site	Telescope/instrument	Detector Size	Plate scale (arcsec pixel ⁻¹)	Filters
CTIO	PROMPT/CCD	1024 × 1024	0.600	<i>BV</i>
La Silla	NTT/EFOSC	1024 × 1024	0.240	<i>UBVgr</i>
CTIO	1-m LCOGT-005/SBIG	2048 × 2048	0.467	<i>UBVgri</i>
SSO	1-m LCOGT-003/SBIG	2048 × 2048	0.467	<i>UBVgri</i>
SAAO	1-m LCOGT-010/SBIG	2048 × 2048	0.467	<i>UBVgri</i>
SSO	1-m LCOGT-011/SBIG	2048 × 2048	0.467	<i>UBVgri</i>
SAAO	1-m LCOGT-012/SBIG	2048 × 2048	0.467	<i>UBVgri</i>
SAAO	1-m LCOGT-013/SBIG	2048 × 2048	0.467	<i>UBVgri</i>
La Silla	NTT/SoFI	1048 × 1048	0.288	<i>JHK_s</i>

Table 2. Peak magnitude information for SN 2015F.

Filter	MJD peak (days)	Peak magnitude	Δm_{15}
<i>U</i>	57106.15(0.06)	13.25(0.03)	1.55(0.04)
<i>B</i>	57106.45(0.02)	13.46(0.03)	1.35(0.03)
<i>V</i>	57108.36(0.03)	13.27(0.02)	0.76(0.02)
<i>g</i>	57107.20(0.01)	13.38(0.03)	1.00(0.03)
<i>r</i>	57107.88(0.01)	13.26(0.01)	0.68(0.01)
<i>i</i>	57104.28(0.02)	13.61(0.01)	0.54(0.01)
<i>J</i>	57102.30(1.00)	13.32(0.06)	–
<i>H</i>	57100.23(1.00)	13.46(0.06)	–
<i>K_s</i>	57103.91(1.00)	13.25(0.06)	–

Numbers in parenthesis correspond to 1- σ statistical uncertainties.

(Krisciunas et al. 2004) of SN 2015F. The $E(B - V)_{\text{host}}$ values derived using different methods are in good agreement with each other, and the weighted average is $E(B - V)_{\text{host}} = 0.085 \pm 0.019$ mag; the uncertainty corresponds to the standard deviation from the weighted average.

2.1.1 Distance to NGC 2442

We used the peak magnitudes of SN 2015F to estimate the distance to its host galaxy, NGC 2442 (Table 4). We corrected the observed peak magnitudes for Milky way and host-galaxy extinction assuming a Cardelli et al. (1989) reddening law (with $R_V = 3.1$). We estimated the absolute peak magnitudes of SN 2015F using the Phillips et al. (1999) and Kattner et al. (2012) decline rate/peak luminosity calibrations in the optical and in the NIR, respectively. We assumed $H_0 = 70 \text{ km s}^{-1} \text{ Mpc}^{-1}$ and, somewhat arbitrarily, an uncertainty of $3.0 \text{ km s}^{-1} \text{ Mpc}^{-1}$, placing H_0 and its uncertainty between the two currently popular values of $67.3 \pm 1.2 \text{ km s}^{-1} \text{ Mpc}^{-1}$ (Planck Collaboration et al. 2014) and $73.03 \pm 1.79 \text{ km s}^{-1} \text{ Mpc}^{-1}$ (Riess et al. 2016). The 1σ uncertainty in H_0 corresponds to an uncertainty of ≈ 4 per cent in distance (0.1 mag).

Table 4 also lists distance estimates from the literature, including Im et al. (2015) distance estimate to NGC 2442 also using SN 2015F. Im et al. (2015) measured a host galaxy extinction of $E(B - V)_{\text{host}} = 0.035 \pm 0.033$ mag, a peak magnitude of $B_{\text{max}} = 13.36 \pm 0.10$ mag, and a decline rate of $\Delta m_{15}(B) = 1.26 \pm 0.10$ mag using *SNANA* (Kessler et al. 2009) to fit MLCS2k2 templates (Jha et al. 2007) to their observed data of SN 2015F. These light curve parameters are consistent with our values at the 1- to 2- σ level.

Our mean distance modulus in the optical (*BV*-filters) is

$\mu_{\text{optical}} = 31.64 \pm 0.14$, and in the NIR (*JH*-filters) is $\mu_{\text{NIR}} = 31.68 \pm 0.11$, where the uncertainties include filter-to-filter peak magnitude covariances. These are in excellent agreement, and are consistent with the Tully et al. (2009) distance estimation based on the Tully-Fisher relation. Our mean distance estimates in the optical and NIR are 1.7- and 1.8- σ discrepant from the Im et al. (2015) distance modulus value, respectively. Im et al. (2015) quote an uncertainty of 0.04 mag in the distance modulus to NGC 2442, which appears underestimated when compared with their quoted uncertainty in the *B*-band peak magnitude (0.10 mag), and the typical dispersion in the absolute magnitudes of SNe Ia in the optical (0.12 to 0.16 mag; Folatelli et al. 2010).

2.1.2 Rise time and Epoch of First Light

Early observations are fundamental to place constraints on several properties of SNe Ia, such as the time of the explosion (Nugent et al. 2011; Hachinger et al. 2013; Zheng et al. 2013; Mazzali et al. 2014; Goobar et al. 2014; Zheng et al. 2014; Marion et al. 2016; Shappee et al. 2016), the radius of the progenitor (Nugent et al. 2011; Bloom et al. 2012), and to search for signs of, or rule out an interaction of the SN ejecta with a companion star (Kasen 2010; Hayden et al. 2010; Bianco et al. 2011; Brown et al. 2012; Goobar et al. 2014; Cao et al. 2015; Olling et al. 2015; Goobar et al. 2015; Im et al. 2015; Marion et al. 2016; Shappee et al. 2016). Here, using the early *V*-band observations of SN 2015F, we place strong constraints on the epoch of first light, the time when the first photons diffuse out from the SN ejecta. Recent very early abundance tomography of SN 2010jn (Hachinger et al. 2013) and SN 2011fe (Mazzali et al. 2014) shows that this estimated epoch of first light is in tension with the time of the explosion derived from spectral modelling, implying a dark phase for these two SNe of the order of ≈ 1 d between the time of the explosion and the emergence of the first photons.

A non-detection of SN 2015F in the *R*-band was reported by Im et al. (2015) on MJD 57088.511, and the first unambiguous detection ($>3\sigma$) on MJD 57089.463, 22.84 h later. Im et al. (2015) also discuss a possible 2- σ detection of emission from the cooling of the shocked heated ejecta (Piro et al. 2010; Rabinak & Waxman 2011) around three days before the first clear detection. Here, we report 3- σ non-detections to a limiting magnitude of 19.017 and 18.709 in the *V*-band on MJD 57089.073 and MJD 57089.184, 9.35 h and 6.69 h before the first detection of Im et al. (2015) in the *R*-band. Our first detection of *V* = 18.055 \pm 0.101 is on MJD 57090.124, 15.87 h after the first detection of Im et al. (2015), and 22.56 h after our last non-detection.

We use a parameterization of $f_{\text{model}} = \alpha(t - t_0)^n$ to fit the rising

Table 3. Host galaxy reddening along the line-of-sight to SN 2015F.

Method	$E(B - V)_{\text{host}}$	Reference
$E(B - V)_{\text{tail}}$	0.110(0.050)	Phillips et al. (1999)
$B_{\text{max}} - V_{\text{max}}$	0.066(0.039)	Phillips et al. (1999)
$V - H$	0.080(0.037)	Krisciunas et al. (2004)
$V - K$	0.093(0.038)	Krisciunas et al. (2004)
Mean	0.085(0.019)	

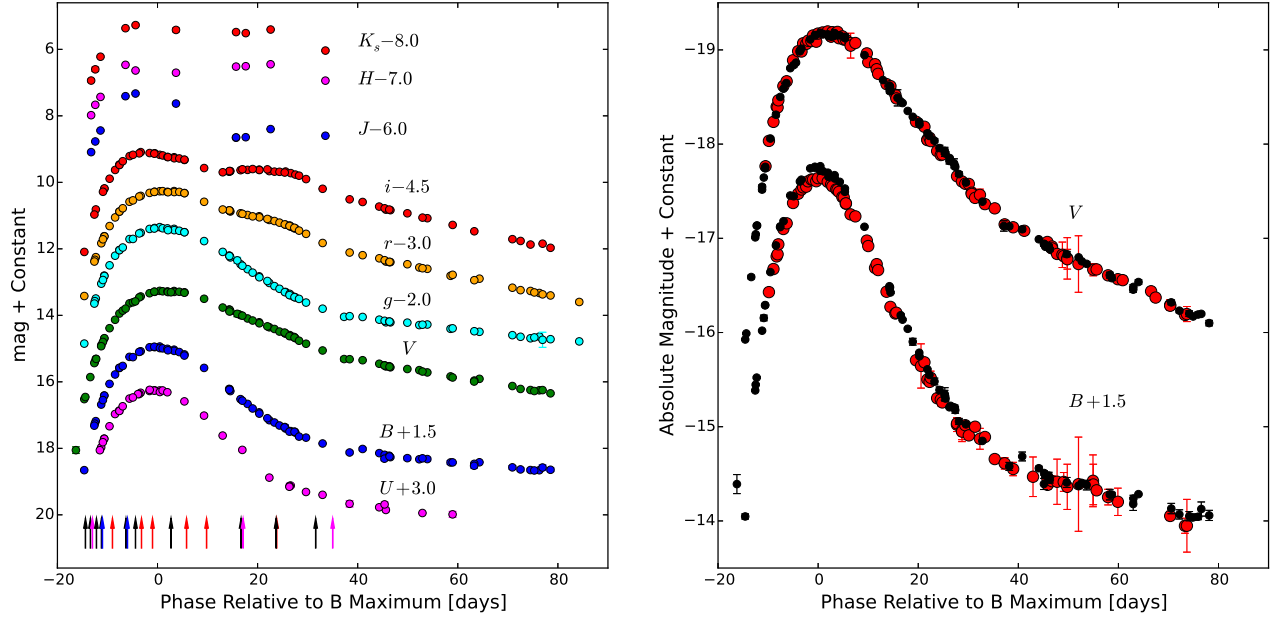


Figure 2. *Left-panel:* The observed $UBVGriJHK_s$ light curves of SN 2015F. The light curves are offset as indicated for clarity. The vertical arrows indicate the epochs of the optical spectra, and are colour-coded to indicate different instruments as in Fig. 4. No corrections for extinction have been made. *Right-panel:* A comparison between the BV absolute magnitude light curves of SN 2015F (black circles) and SN 2004eo (red points; Pastorello et al. 2007). We corrected both SNe for extinction; for SN 2004eo we assumed $E(B - V)$ values from Pastorello et al. (2007). Both SNe show remarkably similar light curves, and the main difference between them is that SN 2004eo is slightly fainter by ~ 0.1 mag in M_B .

Table 4. Distance estimates to NGC 2442.

Reference	Distance modulus μ	Distance (Mpc)	Method/ $\Delta m_{15}/M_{\text{max}}$ relation
This paper	31.63(0.20)	21.2(2.0)	SNe Ia/Phillips et al. (1999) B -band calibration
This paper	31.64(0.18)	21.3(1.8)	SNe Ia/Phillips et al. (1999) V -band calibration
This paper	31.68(0.18)	21.7(1.8)	SNe Ia/Kattner et al. (2012) J -band calibration
This paper	31.69(0.14)	21.8(1.4)	SNe Ia/Kattner et al. (2012) H -band calibration
Im et al. (2015)	31.89(0.04)	23.9(0.4)	SNe Ia/ B -band using MLCS2k2 (Jha et al. 2007)
Tully et al. (2009)	31.66(0.17)	21.5(1.7)	Tully-Fisher relation
Tully (1988)	31.16(0.80)	17.1(6.3)	Tully-Fisher relation

V -band light curve, described in detail in Firth et al. (2015), where t_0 is the time of first light, α is a normalizing coefficient, and n is the index of the power law. The case of $n = 2$ is known as the ‘expanding fireball’ model (e.g., Riess et al. 1999). The early V -band light curve, together with the best fit model, is shown in Fig. 3.

We find best fit parameters of $t_0 = 57088.394^{+0.076}_{-0.074}$, and $n = 2.20^{+0.03}_{-0.03}$. The V -band rise time, corrected for time dilation, is $t_{\text{rise}} = 19.87 \pm 0.08$ d. The mean values obtained by Firth et al. (2015), for a

sample of 18 SNe Ia with well-sampled early light curves from the Palomar Transient Factory (PTF Law et al. 2009; Rau et al. 2009) observed in the R_{P48} -band, and from La Silla-QUEST (Baltay et al. 2013) in the broad $(g + r)$ -band (see Baltay et al. 2013; Cartier et al. 2015), are $\bar{t}_{\text{rise}} = 18.98 \pm 0.54$ d, and $\bar{n} = 2.44 \pm 0.13$. Firth et al. (2015) showed that the t_{rise} and n in the $(g + r)$ -band is very similar to an optical pseudo-bolometric optical light curve and the R_{P48} -band has a t_{rise} longer by 0.39 d. Firth et al. (2015) also find that t_{rise}

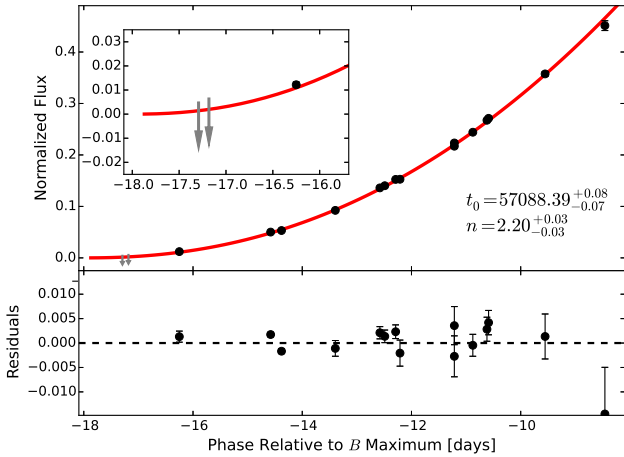


Figure 3. In the top-panel, black points denote the normalized early-time V -band light curve of SN 2015F; the red line corresponds to the best fitted power law model ($f_{\text{norm}} \propto (t - t_0)^n$; see [Firth et al. 2015](#), and Section 2.1.2). Grey arrows correspond to the $3\text{-}\sigma$ upper limits. The lower-panel, shows the residuals from the fit. The SN brightness predicted by the model at the epochs of the upper-limits is consistent with the non-detections (see inset).

is longer by 0.79 d and n is larger by 0.1 in the V -band, compared to an optical pseudo-bolometric light curve. After applying these corrections, the t_{rise} found for SN 2015F is close to the mean value of [Firth et al. \(2015\)](#) sample, and n is $\sim 2\sigma$ lower than the mean value, although still within the range of values found by [Firth et al. \(2015\)](#).

The early photometry of SN 2015F does not show any evidence of shock cooling, such as an excess emission or bluer than normal colours, produced by the interaction of the SN ejecta with a companion star as in SN 2012cg ([Marion et al. 2016](#)). We will analyze in detail possible progenitor scenarios of SN 2015F using the very early phase data presented here in a future work.

2.2 Spectroscopy

We obtained optical spectra of SN 2015F with EFOSC2/NTT, with the Robert Stobie Spectrograph (RSS [Kobulnicky et al. 2003](#)) on the Southern African Large Telescope (SALT), with WiFeS ([Dopita et al. 2010](#)) on the Australian National University (ANU) 2.3-m Telescope, and with the FLOYDS spectrograph on the 2-m Faulkes Telescope South (FTS) at the Siding Spring Observatory. The EFOSC2 spectra were reduced as described in [Smartt et al. \(2015\)](#), and the FLOYDS data were reduced with the FLOYDSPEC pipeline³. The RSS is a long slit spectrograph, the spectra of SN 2015F were reduced using the PYSALT pipeline which is described in detail in [Crawford et al. \(2010\)](#). WiFeS is an integral field unit spectrograph, one dimensional spectra were reduced and extracted from the data cube using a PSF-weighted fit using `pywifis` pipeline ([Childress et al. 2014a](#)). In Table 5 we summarize the optical spectroscopic observations of SN 2015F. We correct all our spectra for Galactic extinction using a [Cardelli et al. \(1989\)](#) extinction law with $R_V = 3.1$, and convert to the rest-frame using the recession velocity of the host galaxy. All reduced PESSTO data

will be available from the ESO Science Archive Facility in Spectroscopic Survey Data Release 3 (SSDR3), due for submission in late 2016. Details will be posted on the PESSTO website⁴. All our spectra are available from the WISEREP archive⁵ ([Yaron & Gal-Yam 2012](#)).

3 SPECTROSCOPIC ANALYSIS

In Fig. 4 we show the spectral sequence of SN 2015F spanning -14 to $+35$ d (throughout, all phases are given relative to maximum light in the rest-frame B -band). The overall characteristics of SN 2015F are those of a normal, if slightly sub-luminous, SN Ia, with properties particularly similar to SN 2004eo (see Fig 2), a transitional object between normal and sub-luminous SNe Ia ([Pastorello et al. 2007](#)). The ratio of the pseudo-equivalent widths (pEW) of the Si II $\lambda 5972$ and Si II $\lambda 6355$ features ($\mathcal{R}(\text{Si II})$; see [Nugent et al. 1995](#); [Bongard et al. 2006](#); [Hachinger et al. 2008](#)) is $\mathcal{R}(\text{Si II}) = 0.31$, measured from the spectrum obtained at $+2$ d. For our $\Delta m_{15}(B) = 1.35$, this is consistent with published relationships between $\mathcal{R}(\text{Si II})$ and $\Delta m_{15}(B)$ (e.g., [Benetti et al. 2005](#); [Blondin et al. 2012](#)).

3.1 Expansion velocities of Si II

In Fig. 5 we present the Si II $\lambda 6355$ velocity (v_{Si}) measured from the minimum of the $\lambda 6355$ Å absorption feature observed near 6150 Å. In the figure, we compare with several low-velocity gradient (LVG) and high-velocity gradient (HVG) SNe Ia⁶. We estimate v_{Si} at maximum light (v_{Si}^0) and \dot{v}_{Si} , by fitting a first degree polynomial to the v_{Si} measurements over -7 to $+30$ d, and interpolating to obtain $v_{\text{Si}}^0 = 10400 \text{ km s}^{-1}$ and $\dot{v}_{\text{Si}} = 50 \text{ km s}^{-1} \text{ d}^{-1}$. These values place SN 2015F in the LVG group.

At phases prior to -10 d, SN 2015F presents a slower v_{Si} than SN 2011fe (see Fig. 5). The difference in v_{Si} between these two SNe at -14 d is $\sim 1000 \text{ km s}^{-1}$. After -10 d, SN 2015F shows a v_{Si} evolution similar to SN 2011fe and SN 2004eo.

3.2 Comparison to other SNe Ia

We next compare in detail the spectra of SN 2015F to other SNe Ia from the literature. We focus our analysis at phases earlier than -10 d, and also make a comparison to sub-luminous SN 1991bg-like SNe Ia.

3.2.1 Comparison at -14 days

The top-left panel of Fig. 6 compares the first spectrum of SN 2015F at -14 d, with SN 2011fe and SN 1990N at a similar phase. We also show the spectra of SN 2011fe at -16.6 d and -16.3 d ([Nugent et al. 2011](#)). SN 2011fe is a normal brightness SN Ia ($\Delta m_{15}(B) = 1.10$; [Pereira et al. 2013](#)) while SN 1990N is relatively bright among the group of normal (i.e., non SN 1991T-like) SNe Ia, with $\Delta m_{15}(B) = 1.03$ ([Lira et al. 1998](#)). Most of the

⁴ <http://www.pessto.org>

⁵ <http://wiserep.weizmann.ac.il/>

⁶ [Benetti et al. \(2005\)](#) separated SNe Ia into three groups: High-velocity gradient (HVG) events, consisting of objects with a velocity gradient of Si II $\lambda 6355$ $\dot{v}_{\text{Si}} \geq 70 \text{ km s}^{-1} \text{ d}^{-1}$ and $\Delta m_{15}(B) \leq 1.5$, low-velocity gradient (LVG) events, consisting of objects with $\dot{v}_{\text{Si}} \leq 70 \text{ km s}^{-1} \text{ d}^{-1}$ and $\Delta m_{15}(B) \leq 1.5$, and FAINT events with $\Delta m_{15}(B) \geq 1.5$.

³ <https://www.authorea.com/users/598/articles/6566>

Table 5. Summary of spectroscopic observations of SN 2015F.

Date UT	MJD (days)	Phase (days)	Instrument/ telescope	Wavelength range (Å)	Resolution (Å)	Exposure time (s)
20150311	57092.0	-14.4	EFOSC/NTT	3646 - 9238	18	300
20150312	57093.0	-13.4	EFOSC/NTT	3346 - 9987	14	1500
20150312	57093.4	-13.0	WiFeS/ANU 2.3-m	3500 - 9565	1.2	1200
20150313	57094.2	-12.2	EFOSC/NTT	3343 - 9985	14	1500
20150314	57095.2	-11.2	EFOSC/NTT	3343 - 9983	14	600
20150314	57095.4	-11.0	FLOYDS/FTS	3200 - 9997	12	1800
20150316	57097.4	-9.0	RSS/SALT	3875 - 8091	18	330
20150319	57100.1	-6.3	EFOSC/NTT	3343 - 9985	14	600
20150319	57100.4	-6.0	FLOYDS/FTS	3201 - 9985	12	1800
20150321	57102.0	-4.4	EFOSC/NTT	3346 - 9986	14	600
20150322	57103.3	-3.2	RSS/SALT	3875 - 8091	18	300
20150324	57105.4	-1.0	RSS/SALT	3875 - 8091	18	300
20150328	57109.1	+2.7	EFOSC/NTT	3346 - 9985	14	600
20150331	57112.3	+5.8	RSS/SALT	3875 - 8091	18	300
20150404	57116.3	+9.8	RSS/SALT	3875 - 8091	18	300
20150411	57123.1	+16.7	EFOSC/NTT	3343 - 9983	14	900
20150411	57123.5	+17.1	WiFeS/ANU 2.3-m	3500 - 9565	1.2	2400
20150418	57130.1	+23.7	EFOSC/NTT	3343 - 9984	14	900
20150418	57130.2	+23.8	RSS/SALT	3875 - 8091	18	300
20150426	57138.0	+31.6	EFOSC/NTT	3346 - 9986	14	900
20150429	57141.4	+35.0	WiFeS/ANU 2.3-m	3500 - 9565	1.2	2400

spectral differences can be explained as a mere temperature effect. SN 1990N is brighter/hotter, and shows fewer features in its spectrum, SN 2011fe is at an intermediate luminosity and shows a broadly similar spectrum to SN 2015F, while SN 2015F itself is fainter/cooler and shows more absorption lines below 5500 Å due to singly ionized iron-peak elements.

The top-right panel of Fig. 6 shows the same spectra in the region around the C II $\lambda 6580$ and $\lambda 7234$ lines. In SN 2011fe, a photospheric component of both of these C II lines is clearly observed at $\approx 13000 \text{ km s}^{-1}$ (studied in Parrent et al. 2012). In SN 1990N, the lines have also been reasonably securely identified (e.g., Mazzali 2001). Fisher et al. (1997) proposed that the flat-bottomed absorption feature at $\sim 6000 \text{ Å}$ could also be due to C II $\lambda 6580$, this time at high velocity. Although Mazzali (2001) showed that Si II is responsible for most of this feature (and in particular the extended blue side; see also Mazzali et al. 1993), an additional explanation may be needed for the red side, which could include a carbon shell at 20000 km s^{-1} . The SN 2015F spectrum also shows clear absorption to the red side of the Si II $\lambda 6355$ line, consistent with C II $\lambda 6580$ at $\sim 13000 \text{ km s}^{-1}$, a velocity similar to the photospheric C II lines in SN 2011fe at the same phase (Parrent et al. 2012). The corresponding photospheric C II $\lambda 7234$ can also be seen, although this feature is not strong in SN 2015F.

A broad absorption feature at $\sim 6800 \text{ Å}$ is very clear (top-right Fig. 6). Possible identifications include photospheric Al II, or C II $\lambda 7234$ at 20000 km s^{-1} . There is no indication of a corresponding C II $\lambda 6580$ at about 20000 km s^{-1} , although the inclusion of C II in our modelling yields a slightly better fit to the red side of the Si II $\lambda 6355$ absorption line (see also Cartier et al. 2014). We model the spectra in detail in Section 4, where we consider both possibilities.

3.2.2 Comparison at -11 days

The lower-left panel of Fig. 6 shows the comparison of the LVG SNe Ia SN 2015F, SN 2011fe, SN 2007af, SN 2004eo and SN 2012ht at around -11 d. SN 2015F shows a remarkable simi-

larity to SN 2004eo, with the main difference being the absence of clear C II lines in SN 2004eo (Pastorello et al. 2007; Mazzali et al. 2008). A strong feature in all the spectra is the broad Ca II NIR triplet, extending from ~ 10000 to $\sim 25000 \text{ km s}^{-1}$ (see Section 3.3), with Ca II HK also visible where the spectra extend to the blue. An apparent evolution in the shape and strength of the spectral features with brightness/temperature ($\Delta m_{15}(B)$) is seen in the region dominated by iron-peak elements (wavelengths bluer than $\sim 5500 \text{ Å}$) and in the Ca II NIR triplet; however, overall there is a remarkable degree of spectral similarity in this sample of LVG SNe Ia.

In Fig. 6 we also show the region around C II $\lambda 6580$ and $\lambda 7234$. SN 2015F, SN 2012ht, SN 2011fe and SN 2007af show clear photospheric C II $\lambda 6580$, with SN 2011fe, SN 2007af, and possibly SN 2015F showing clear photospheric C II $\lambda 7234$ absorption (the spectrum of SN 2012ht is too noisy to clearly detect any weak feature). There is also clear absorption at $\sim 6800 \text{ Å}$ present in SN 2015F, SN 2007af and perhaps SN 2004eo, although in this latter case nearby telluric features hamper a convincing identification.

3.2.3 Comparison with SN 1991bg-like type Ia SNe

SN 2015F has some similarities with SN 2004eo (Fig. 2 and 6), a transitional object between normal and sub-luminous SNe Ia (Pastorello et al. 2007; Mazzali et al. 2008). The SN Ia sub-luminous class, often referred to as SN 1991bg-like SNe, are characterized by a fast decline in their light curves (Filippenko et al. 1992), somewhat lower expansion velocities compared to normal SNe Ia (Hachinger et al. 2009; Doull & Baron 2011), a small amount of ^{56}Ni synthesized during the explosion (Mazzali et al. 1997; Höflich et al. 2002; Hachinger et al. 2009), and clear Ti II lines around maximum light (Filippenko et al. 1992; Mazzali et al. 1997; Garnavich et al. 2004; Taubenberger et al. 2008; Doull & Baron 2011).

Fig. 7 compared SN 2015F to a group of well-observed SN 1991bg-like events. Although SN 2015F at -13 d has higher expansion velocities than SN 1991bg-like SNe, with SN 2015F

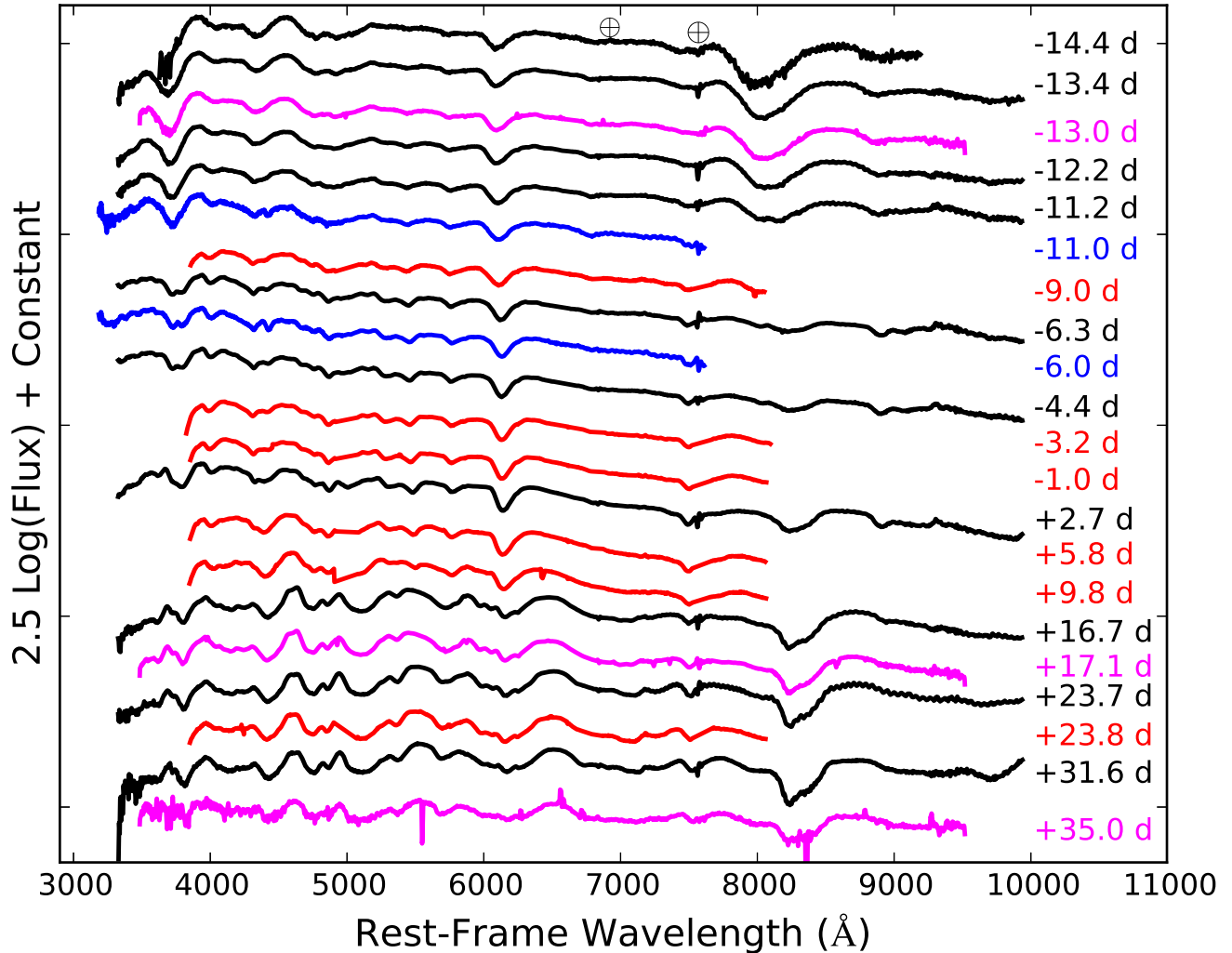


Figure 4. The spectral sequence of SN 2015F. In black we show the spectra obtained with EFOSC2/NTT with PESSTO, in red the spectra obtained using the RSS spectrograph on SALT, in magenta the spectra obtained with WiFeS on the ANU 2.3-m, and in blue the spectra obtained using FLOYDS on the Faulkes Telescope South by the LCOGT network. The phase of the spectrum relative to maximum light in the *B*-band is shown on the right. The position of the main telluric features are also marked. In all figures, the spectra have been corrected for galactic extinction, additionally SN 2015F has been also corrected by host galaxy extinction (Section 2.1).

showing very broad features formed by the blending of several lines, it shares some spectral resemblance to SN 1991bg-like events over 3900–5000 Å. This similarity is a consequence of absorption lines of iron-peak elements such as Ti II, V II and Cr II, with some of these ions commonly identified in SN 1991bg-like SNe (see Doull & Baron 2011).

In Fig. 7 we overplot the spectrum of SN 2015F at -6 d on top of the -13 d spectrum to highlight the evolution of the spectral features. We show in detail the blue part of the spectra, which are dominated by lines of iron-peak elements. In contrast to the spectrum obtained at -13 d that shows Ti II, V II, and Cr II lines, by -6 d lines of Fe III and Si III are present, commonly seen in normal SNe Ia and which imply a higher ionization of the SN ejecta compared to previous epochs.

Fig. 7 also shows a comparison focussed on the 6800 Å feature. Although sometimes weak, this always appears present in SN 1991bg-like objects. The presence of Ti II and Cr II, associated with a low ejecta temperature, may also suggest that the 6800 Å feature is a product of a low ejecta temperature. However, we note that this feature is also present at -6 d and -4 d in SN 2015F, when there are also clear lines of doubly-ionized species (Fe III, Si III), implying a relatively high ejecta temperature. Thus temperature is unlikely to be the only parameter that explains the 6800 Å feature.

The overall appearance of the spectra of SN 2015F around maximum light shows that although SN 2015F shares some similarities with SN 1991bg-like SNe, it should be considered as a member of the group of normal SNe Ia.

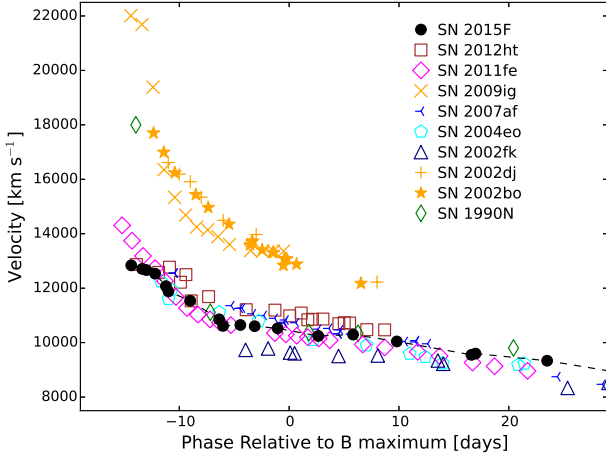


Figure 5. Si II velocities (v_{Si}) measured from the minimum of the Si II $\lambda 6355$ absorption feature for SN 2015F (black circles and dashed line). For comparison we show v_{Si} for the LVG SNe Ia SN 1990N (green diamonds; Leibundgut et al. 1991; Mazzali et al. 1993), SN 2004eo (cyan pentagons; Pastorello et al. 2007; Folatelli et al. 2013), SN 2007af (blue; Blondin et al. 2012; Folatelli et al. 2013), SN 2011fe (magenta diamonds; Pereira et al. 2013), and SN 2012ht (brown squares; Yamanaka et al. 2014). We also show v_{Si} for the HVG SNe Ia SN 2002bo (orange stars; Benetti et al. 2004), SN 2002dj (orange plus symbols; Pignata et al. 2008), and SN 2009ig (orange crosses; Foley et al. 2012; Marion et al. 2013), and for SN 2002fk (dark blue triangles; Cartier et al. 2014), characterized by persistent C II absorption features until past maximum light, and by a low v_{Si} and \dot{v}_{Si} .

3.3 Ca II high-velocity features

The Ca II high velocity (HV) features are strong in the very early spectra of SN 2015F, dominating the Ca II features until a week before maximum light. After these phases the photospheric component becomes dominant, and the HV component disappears around maximum light. In Fig. 8 we show the Ca II H&K and the NIR triplet in velocity space for the -14 d to -11 d spectra. For Ca II H&K, the expansion velocity is calculated with respect to the average wavelength of the H&K lines (3951 \AA), while for the NIR triplet the velocity is with respect to the strongest line (8542 \AA).

Following Childress et al. (2013, 2014b), Maguire et al. (2014) and Silverman et al. (2015), we fit Gaussian profiles to the Ca II lines, defining a pseudo-continuum on either side of the profile, and using it to normalize the spectrum. To model the Ca II NIR feature, we used both HV and photospheric components each composed of three Gaussian profiles with fixed relative positions and a common width. We allowed the relative strength of the three lines to vary, but to be the same for both components. The best-fitting parameters are listed in Table 6 and are shown in Fig. 8. The relative strengths are similar across the different epochs, and close to the theoretical values expected from atomic physics.

The Ca II H&K region is more complex due to additional photospheric Si II at $\lambda 3856$, coupled with blanketing from iron-peak elements that makes the definition of the pseudo-continuum less reliable. Following Maguire et al. (2014) and Silverman et al. (2015), we modelled each pair of Ca II H&K lines using two Gaussians where the relative positions and their widths were fixed, and the relative strength of the two Gaussians fixed to unity. We consider the HV and photospheric Ca II components, the Si II $\lambda 3856$ line, and a weak feature at $\sim 3600 \text{ \AA}$, possibly caused by the blending

of several lines of iron-peak elements (the feature can be seen at $\sim 27000 \text{ km s}^{-1}$ in Fig. 8). We fixed the position of the Si II $\lambda 3856$ line to be within 5 per cent of the photospheric velocity of the Ca II NIR line, and the velocity of the Ca II H&K HV and photospheric components to be within 10 per cent of the values from the Ca II NIR lines.

The Si II feature is required in our fits from -11 d. The weak feature at $\sim 3600 \text{ \AA}$ is blended with the Ca II H&K line at early stages, but around maximum light the feature becomes more detached, becoming an independent feature on the blue side of the H&K profile around peak brightness. The extension of the Ca II material reaches a velocity of $\sim 29000 \text{ km s}^{-1}$ in the very outermost layers of SN 2015F.

3.3.1 Velocity evolution of Ca II

Fig. 9 shows the expansion velocity of the Ca II lines as function of phase. The median difference between the HV and the photospheric components for the NIR and H&K features is 7850 km s^{-1} and 7350 km s^{-1} , respectively, consistent with previous studies using larger samples (Maguire et al. 2014; Silverman et al. 2015). The HV Ca II component shows a dramatic velocity evolution over -14 d to -11 d, evolving from 23000 km s^{-1} to 19500 km s^{-1} in three days. It then plateaus, decreasing only $\sim 500 \text{ km s}^{-1}$ over the next five days. This plateau is coincident with a transition from equally strong HV and photospheric components, to a dominant photospheric component (see Table 6). After -6 d, the velocity of the HV Ca II again declines more rapidly.

We find a very good agreement between the Si II $\lambda 6355$ velocity (measured from the minimum of the feature) and the Ca II photospheric velocities (measured with the Gaussian fitting), remarkable as the techniques are quite independent. Only at epochs prior to -11 d do we see a departure in the behaviour of the Si II velocity from the Ca II photospheric velocity, with the Si II showing a shallower evolution; this may be the result of contamination from HV C II $\lambda 6580$ moving the minimum of the line profile to redder wavelengths.

Finally, we see a different behaviour in the velocity evolution of the HV Ca II and photospheric lines, and the 6800 \AA absorption feature (Fig. 9). While the other lines show a consistent evolution, the 6800 \AA feature shows a evolution similar to a plateau with a small slope. We note that the velocity measurement at -6 d is hampered by a nearby telluric line, and at later epochs the minimum of the feature is strongly affected by telluric absorption.

3.3.2 Strength of the Ca II features

Childress et al. (2014b) defined R_{HVF} as the ratio between the pEWs of the HV and photospheric Ca II NIR components. In Table 6 we list the evolution of R_{HVF} as function of phase. The HV component is dominant over the photospheric feature from -13 to -11 d, and then declines in strength. At phases later than -10 to -7 d, the ‘photospheric’ Ca II component begins to dominate. Close to maximum light, SN 2015F has $R_{\text{HVF}} \approx 0.23$ consistent with the results of Childress et al. (2014b) and Maguire et al. (2014). In particular, the R_{HVF} value for SN 2015F, and its $\Delta m_{15}(B) = 1.35$, perfectly fits in figure 2 of Childress et al. (2014b).

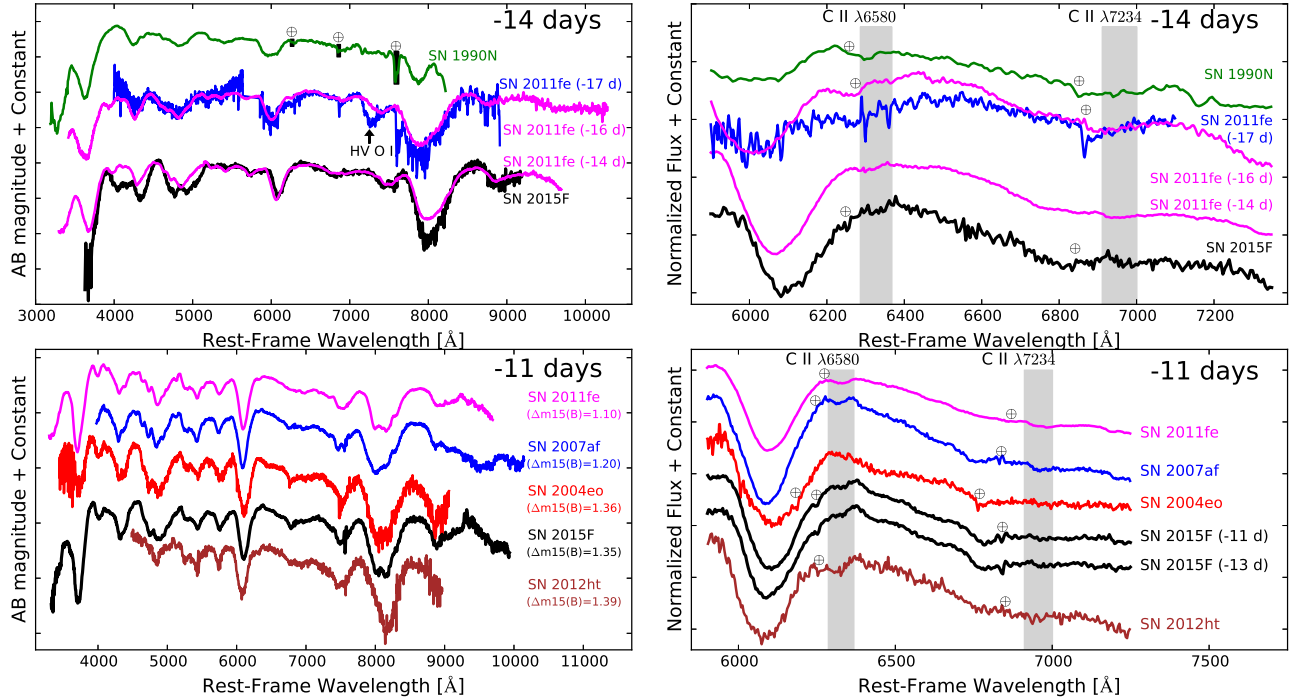


Figure 6. *Top left:* The spectra of SN 2015F (black), SN 1990N (green; [Leibundgut et al. 1991](#)), and SN 2011fe (magenta; [Pereira et al. 2013](#)) at -14 d. We show for comparison the spectra of SN 2011fe at -16.6 d and -16.3 d in blue and magenta ([Nugent et al. 2011](#)), respectively, overplotted to emphasise the high-velocity O I feature, marked with an arrow. We overplotted SN 2011fe on top of SN 2015F to highlight the similarities and differences. Telluric features are marked with an Earth symbol, and in SN 1990N a black rectangle denotes their characteristic width. *Top right:* As top-left, but focussing on the region around C II $\lambda 6580$ and $\lambda 7234$ at -14 d. *Lower left:* A comparison between the spectra of SN 2015F, SN 2004eo (red; [Pastorello et al. 2007](#)), SN 2007af (blue; [Folatelli et al. 2013](#)), SN 2011fe (magenta; [Pereira et al. 2013](#)), and SN 2012ht (brown; [Yamanaka et al. 2014](#)) at ≈ -11 d. The decline rate $\Delta m_{15}(B)$ is indicated on the right. *Lower right:* as lower left, but focussing on the spectral region around C II $\lambda 6580$ and $\lambda 7234$. In the right panels, the grey region marks the position of photospheric C II at an expansion velocity of $10000\text{--}14000$ km s $^{-1}$.

Table 6. Parameters of the Gaussian fits to the Ca II NIR triplet.

Phase [Days]	HVF Component			Photospheric Component			Relative Strengths of		R_{HVF}
	v [km s $^{-1}$]	FWHM [km s $^{-1}$]	pEW [Å]	v [km s $^{-1}$]	FWHM [km s $^{-1}$]	pEW [Å]	Ca II($\lambda 8542$)/ Ca II($\lambda 8662$)	Ca II($\lambda 8498$)/ Ca II($\lambda 8662$)	
-14.4	23236.0	6425.3	171.6	14794.5	9979.5	238.2	1.31	0.23	0.72
-13.4	22109.1	6548.3	177.1	14049.0	8251.9	197.5	1.09	0.10	0.90
-13.0	21124.2	6979.0	186.8	13119.9	7037.0	156.2	1.12	0.14	1.20
-12.2	20130.9	6874.3	185.1	12288.4	6218.9	135.1	1.12	0.23	1.37
-11.2	19671.6	6497.7	148.9	11886.6	5407.1	110.0	1.12	0.23	1.35
-6.3	19046.4	5867.3	64.3	11031.6	5187.0	90.0	1.10	0.23	0.71
-4.4	18436.0	6681.7	58.9	10732.1	5103.7	96.0	1.05	0.15	0.61
$+2.7$	16578.8	5091.3	37.6	10370.4	6877.8	163.0	1.19	0.20	0.23

3.4 C II in SN 2015F

In Fig. 10, we present the spectral sequence of SN 2015F around the C II $\lambda 6580$ and $\lambda 7234$ lines in velocity space, compared to SN 2011fe. The C II $\lambda 6580$ photospheric absorption is detected until -4 d at velocities similar to Si II (see Fig. 9), although the measurement is difficult at phases prior to -10 d as the feature does not have a well defined minimum; see Fig. 10). We also note that around maximum light, the Si II $\lambda 6355$ line becomes stronger while the C II lines become weaker; thus P-Cygni emission from Si II may affect the C II feature by moving the minimum to redder wavelengths (lower velocities).

Fig. 10 also presents a spectral sequence showing the evolution of the ~ 6800 Å absorption feature. One interpretation for this feature is that it is HV C II, which we discuss in Section 5.2.

4 SPECTRAL MODELLING

We next investigate whether simple spectral modelling can assist with further identification of the lines in the spectra of SN 2015F. We used SYN++ ([Thomas et al. 2011b](#)), an updated version of SYNOW ([Fisher et al. 1997](#)), to model the spectra. The physical assumptions of SYN++ match those of SYNOW ([Fisher 2000](#)), so our

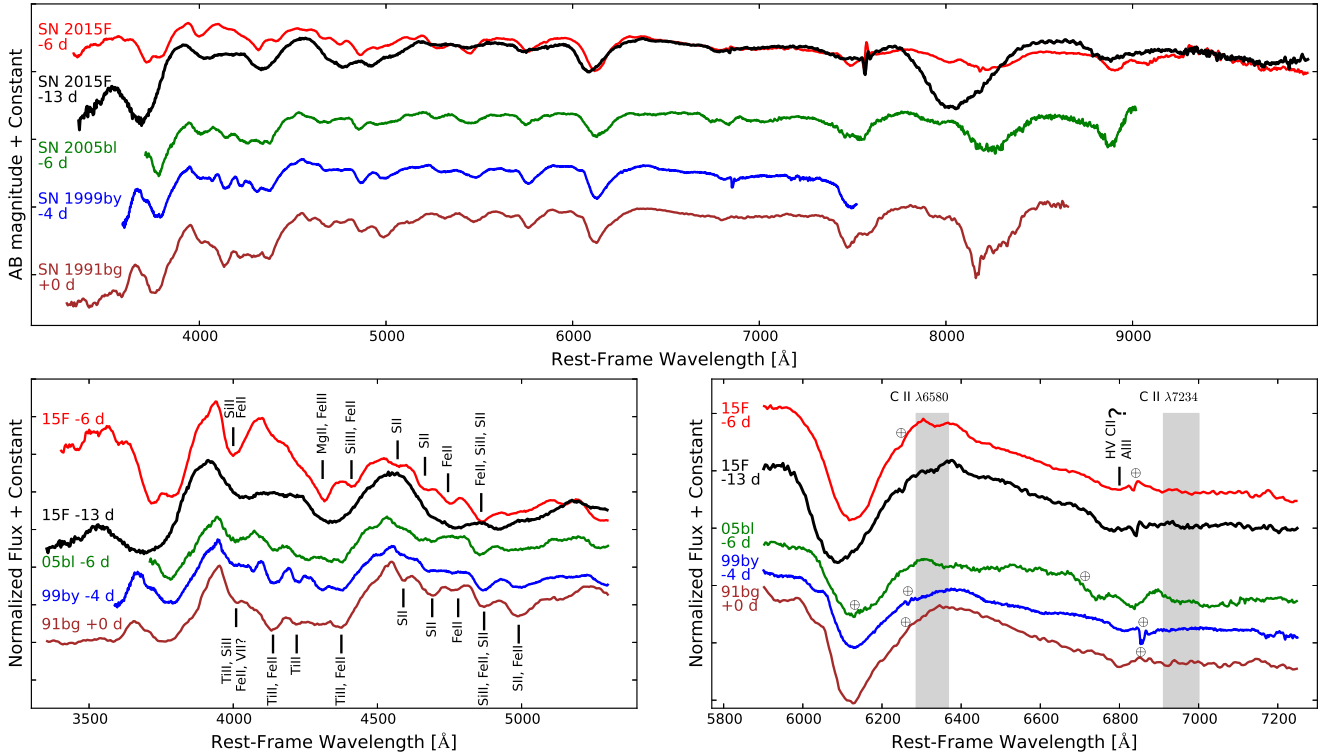


Figure 7. *Top* : The comparison between SN 2015F at -13 d (black), SN 2015F at -6 d (grey), SN 1999by at -4 d (blue; Garnavich et al. 2004), and SN 1991bg at maximum light (brown; Filippenko et al. 1992). *Lower-left*: As in the top panel, but now centred on the region 3300–5400 Å and including the SN 1991bg-like SN 2005bl at -6 d (green; Taubenberger et al. 2008). In this spectral region, SNe Ia display several lines of iron-peak elements, and Ti II lines are a distinctive feature of SN 1991bg-like SNe near to maximum light. *Lower right*: As lower left, but focussing on the region around the 6800 Å feature. The ions responsible for prominent spectral features are indicated.

findings are restricted to the identification of features and not quantitative abundances.

In Fig. 11 we show the spectrum of SN 2015F at -13 d along with a *syn++* model that reproduces the main spectroscopic features reasonably well. We assumed a photosphere expanding at a velocity of 12000 km s⁻¹ and a black body temperature of 9500 K, and allowed various individual ions to be detached from the photosphere; Table 7 lists the velocities and e-folding length scales of the main ions in our models at three representative phases; -13 d, -11 d and -4 d. We note that to reproduce the -13 d spectrum over the region from 4000 to 5000 Å, we required V II, Ti II, Cr II and a significant amount of Fe II at 14800 km s⁻¹. The lines of these iron group elements are therefore produced at a significantly higher velocity than the photosphere, and the e-folding length-scale of Fe II is relatively large (2300 km s⁻¹). This suggests that iron-group material extends well beyond the photosphere, possibly reaching expansion velocities of ~ 20000 km s⁻¹. In Fig. 11, we also present various *syn++* models with different combinations of the iron group lines to show the contribution of these ions in the final model.

In Fig. 12 we overplot our *syn++* models on top of the first four spectra of SN 2015F, and focus on the blue part of the spectra, which are dominated by lines of iron-peak elements. At -14 d and -13 d, the features are very broad, and the spectra exhibit strong absorption features from 3900–4500 Å mainly produced by iron-peak elements. At -12 d the strength of the V II, Ti II and Cr II lines begin to decrease. At -11 d the line profiles become narrower, and

the features produced by V II, Ti II and Cr II are no longer clear. Lines of Fe III, and possibly Si III, begin to appear.

The strong absorption at ~6800 Å can be reproduced by a HV C II component at 20000 km s⁻¹, or by photospheric Al II at a velocity of 13000 km s⁻¹. For the HV C II component, we adjusted $T_{\text{ext}} = 14000$ K to make the HV C II $\lambda 7234$ line stronger than the HV C II $\lambda 6580$ line, thus mimicking as closely as possible the profile in the SN 2015F spectrum. However, as for the $\mathcal{R}(\text{Si II})$ ratio, non-LTE effects may play a role (see Nugent et al. 1995; Hachinger et al. 2008). These are not captured by the LTE assumption of *syn++*, and therefore the T_{ext} used for the HV C II component might not be a reliable estimation of the true value. Even after this adjustment in T_{ext} , the HV C II only partially reproduces the strong absorption feature seen at ~6800 Å. A stronger HV component of C II $\lambda 7234$ and C II $\lambda 4267$ may yield a better model of the ~6800 Å and the ~4030 Å absorption features, respectively.

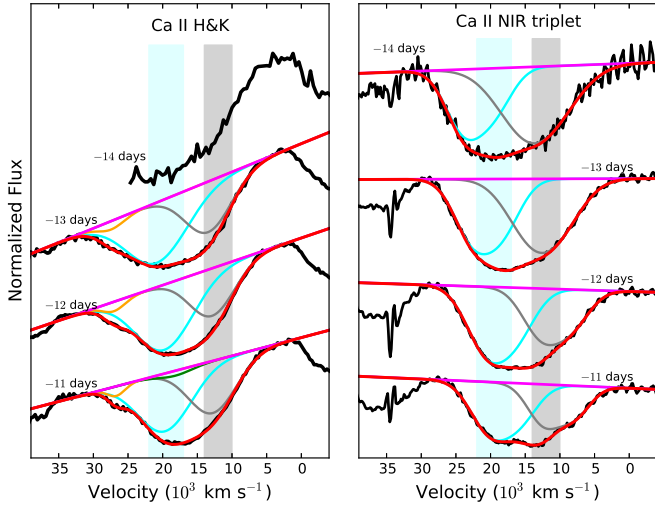
A combination of a HV C II component and of Al II line is also a possibility to explain the ~6800 Å feature, but in terms of *syn++* modelling difficult to disentangle since it yields similar results to the models displayed in Fig. 11.

5 DISCUSSION

The previous sections have presented a high-quality time-series of spectra and photometry of the nearby type Ia SN 2015F. Our data make it one of the best observed SNe Ia at early times, and the early spectroscopic coverage have allowed us to study the outer layers of

Table 7. The SYN++ parameters for the spectral fits at −13 d, −11 d, and −4 d.

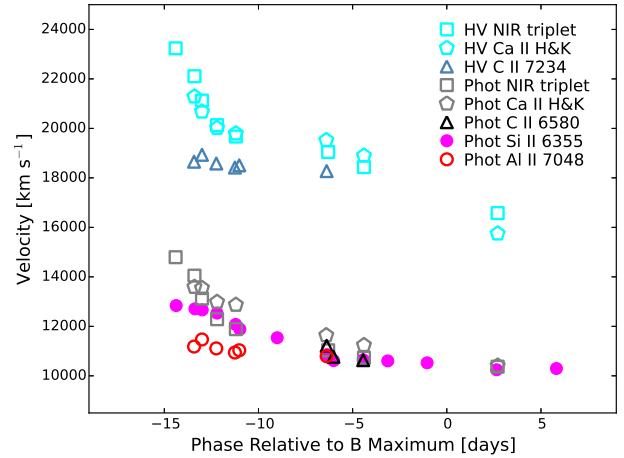
Ion	−13 d model			−11 d model			−4 d model		
	v_{\min} [10^3 km s^{-1}]	T_{ext} [10^3 K]	v_e [10^3 km s^{-1}]	v_{\min} [10^3 km s^{-1}]	T_{ext} [10^3 K]	v_e [10^3 km s^{-1}]	v_{\min} [10^3 km s^{-1}]	T_{ext} [10^3 K]	v_e [10^3 km s^{-1}]
Photosphere	12.0	9.5	...	11.5	10.0	...	10.0	11.5	...
C II	14.0	9.5	1.30	13.5	10.0	1.30	11.5	11.5	1.0
O I	13.0	9.5	2.50	12.5	10.0	1.50	12.5	11.5	1.0
Na I	12.0	9.5	1.00	11.5	10.0	1.00	10.0	11.5	1.0
Mg II	13.0	9.5	1.50	12.5	10.0	1.50	12.5	11.5	1.0
Si II	13.6	9.5	1.90	12.9	10.0	1.80	11.5	11.5	1.7
Si III	10.0	11.5	1.0
S II	12.1	9.5	1.35	11.7	10.0	1.30	11.0	11.5	1.0
Ca II	13.0	9.0	4.00	13.3	10.0	2.00	11.0	11.5	1.5
HV Ca II	20.0	10.0	3.00	18.5	11.5	1.5
Ti II	14.8	9.5	1.80	13.5	10.0	1.50
V II	14.8	9.5	2.00	14.8	10.0	2.00
Cr II	14.8	9.5	2.00
Fe II	14.8	9.5	2.30	12.5	10.0	1.50	11.5	11.5	2.0
Fe III	12.0	10.0	1.50	10.0	11.5	1.0
Al II	13.0	9.5	1.50	12.3	10.0	1.50	12.0	11.5	1.0
HV C II	20.0	14.0	2.10	20.0	14.0	2.10	19.6	14.0	2.0

**Figure 8.** The spectral region around the Ca II H&K lines (left panel) and the NIR triplet (right panel) for SN 2015F at phases < −10 d. The magenta line corresponds to the pseudo-continuum, and the red profile is the resultant model from fitting Gaussian profiles to the observed spectrum. The profiles of the individual HV and photospheric components are shown in cyan and grey, respectively. In the left-panel the Si II $\lambda 3856$ line is shown in green, and the $\sim 3600 \text{ \AA}$ feature in orange. The grey and cyan regions mark the positions of the photospheric ($10000\text{--}14000 \text{ km s}^{-1}$) and HV ($17000\text{--}22000 \text{ km s}^{-1}$) components.

the SN ejecta in detail. In particular, these data provide evidence for either photospheric Al II or high-velocity C II, as well as iron-peak elements in the outer layers. We discuss these in turn.

5.1 Photospheric Aluminium

Our favoured explanation of the $\sim 6800 \text{ \AA}$ spectral feature in SN 2015F is photospheric Al II (see Section 4), expanding at a velocity of $\sim 13000 \text{ km s}^{-1}$ (Fig. 9). The Al II material has to be con-

**Figure 9.** The expansion velocities for different ions in SN 2015F as a function of phase: HV Ca II NIR triplet (cyan squares), HV Ca II H&K (cyan pentagons), photospheric Ca II NIR triplet (grey squares), photospheric Ca II H&K (grey pentagons), Si II $\lambda 6355$ (magenta dots), and photospheric C II $\lambda 6580$ (black triangles). We also show the 6800 \AA line interpreted as either photospheric Al II (open circles) and HV C II (blue triangles).

finned in a relatively narrow range of velocity, as the $\sim 6800 \text{ \AA}$ feature does not appear to evolve in velocity over 16 days (Fig. 10). However, we caution that the feature is quite weak and is affected by telluric absorption; a definitive statement about the velocity evolution is difficult to make.

Aluminium in SNe Ia has not been commonly reported in the literature. To our knowledge, the only previous claim was in the peculiar ‘Ia’ (Bildsten et al. 2007) candidate SN 2010X (Kasliwal et al. 2010). ^{27}Al is the only stable aluminium isotope, which according to nucleosynthesis calculations is $\sim 10^3$ more abundant than the radioactive ^{26}Al isotope (Iwamoto et al. 1999; Seitenzahl et al. 2013). However, the expected mass fraction of

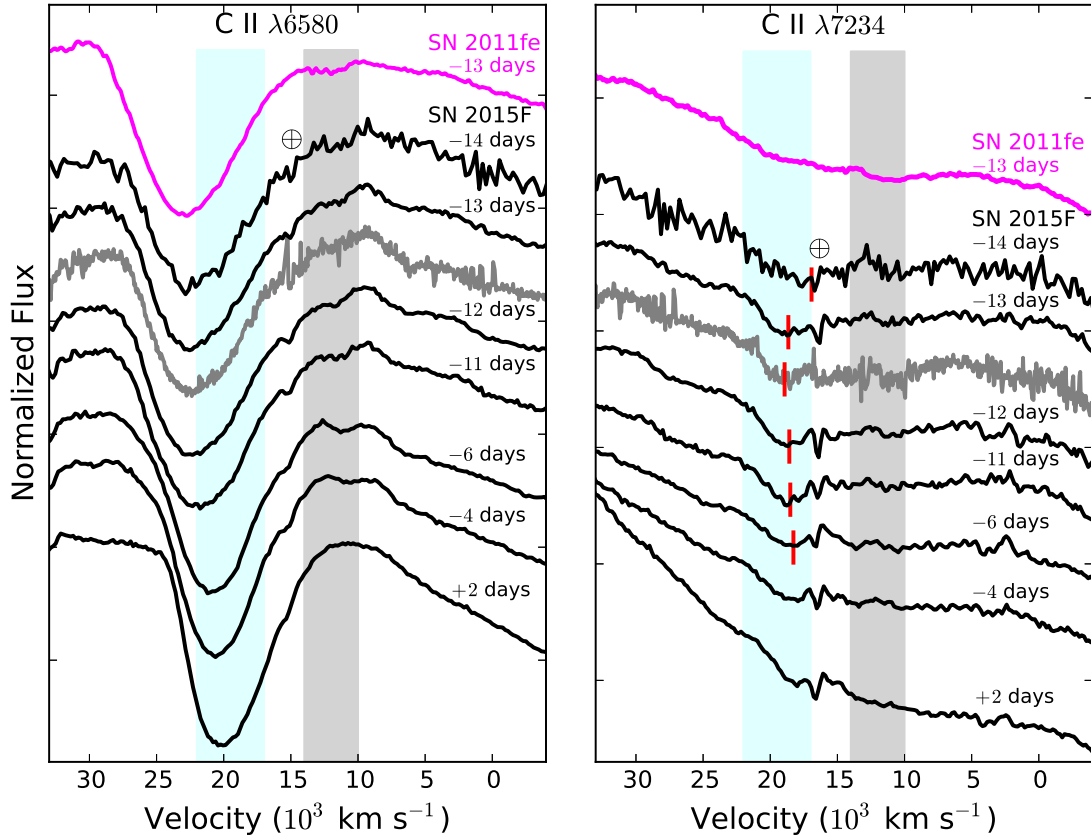


Figure 10. The spectral region around C II $\lambda 6580$ (left panel) and $\lambda 7234$ (right panel) in velocity space. The spectra obtained with EFOSC/NTT are shown in black, and in grey the WiFeS/ANU 2.3-m spectrum at -13 d. In the right panel, the red vertical lines mark the velocity measured from the minimum of the 6800 \AA feature. For comparison, we show the -13 d spectrum of SN 2011fe (magenta). The grey and cyan regions mark the position of the C II lines moving at $10000\text{--}14000 \text{ km s}^{-1}$ (photospheric) and at $17000\text{--}22000 \text{ km s}^{-1}$ (HV).

^{27}Al in SNe Ia is relatively low, only 10^{-3} to 10^{-2} times the total mass of ^{28}Si (Iwamoto et al. 1999; Seitenzahl et al. 2013), the latter being the most abundant silicon isotope in SNe Ia.

Given this low predicted abundance of Al, strong Al II features seem unexpected. The yield of ^{27}Al obtained from the W7 (Nomoto et al. 1984) nucleosynthesis models of Iwamoto et al. (1999), and the three-dimensional N100 delayed-detonation models of Seitenzahl et al. (2013), predict a strong dependence of the abundance of ^{27}Al on metallicity. A change from zero to solar metallicity in the progenitor white dwarf produces an increase of an order of magnitude in the yield of ^{27}Al by mass. As a comparison, the abundances of ^{12}C and ^{28}Si remain essentially flat as function of progenitor metallicity. Thus a relatively metal-rich progenitor may help to explain the presence of Al in SN 2015F.

In Section 3.2 we noted the common presence of the $\sim 6800 \text{ \AA}$ feature in SN 1991bg-like SNe. This class appears to explode in more massive, higher metallicity galaxies; we also note the non-detection of this feature in SN 2011fe which seems to be the result of a sub-solar metallicity progenitor (see Mazzali et al. 2014). As SN 1991bg-like SNe exhibit lower photospheric temperatures than normal SNe Ia, in principle, the presence of the Al II lines could be explained by a temperature effect and not as a metallicity effect. However, in the case of SN 2015F a temperature effect can be ruled out by the simultaneous detection of the $\sim 6800 \text{ \AA}$ feature with Si III lines, which are a signature of a hot SN ejecta, and are strong at -6 d and -4 d (see Section 3.2.3).

5.2 Carbon material

A second explanation for the $\sim 6800 \text{ \AA}$ feature is high-velocity (HV) C II $\lambda 7234$; photospheric C II is clearly detected. This suggests that the outermost layers ($\gtrsim 18000 \text{ km s}^{-1}$) of SN 2015F are mostly unburned, consistent with the Mazzali et al. (2014) model for SN 2011fe, in which the outermost layers of the SN ejecta ($> 19400 \text{ km s}^{-1}$) are unburned, and are composed mainly of carbon. The fact that SN 2015F has a faster decline rate than SN 2011fe, and is thus a dimmer/cooler event, suggests a less efficient burning, and perhaps an even larger amount of unburned material in the outer layers than in SN 2011fe.

In recent delayed-detonation models (Seitenzahl et al. 2013), the outermost layers of the ejecta ($v_{\text{exp}} > 20000 \text{ km s}^{-1}$) are mostly composed of carbon and oxygen, and this may explain any HV C II. Nevertheless, we do not see a correspondingly strong HV O I line in SN 2015F. In Seitenzahl et al. (2013), carbon could also be present down to about 10000 km s^{-1} , which may explain photospheric C II in SN 2015F (but see also Mazzali et al. 2014).

Under the assumption that the 6800 \AA absorption feature corresponds to HV C II $\lambda 7234$, we show its velocity evolution in Figs. 9 and 10. The first spectrum of SN 2015F has lower signal-to-noise ratio implying a larger uncertainty in the minimum of the feature, located at $\approx 16900 \text{ km s}^{-1}$ (6828 \AA). The feature evolves getting weaker and moving to redder wavelengths with time. We measured the minimum of this absorption feature at phases < -6 d (note the measurement is affected by telluric on the red side; see Fig. 10),

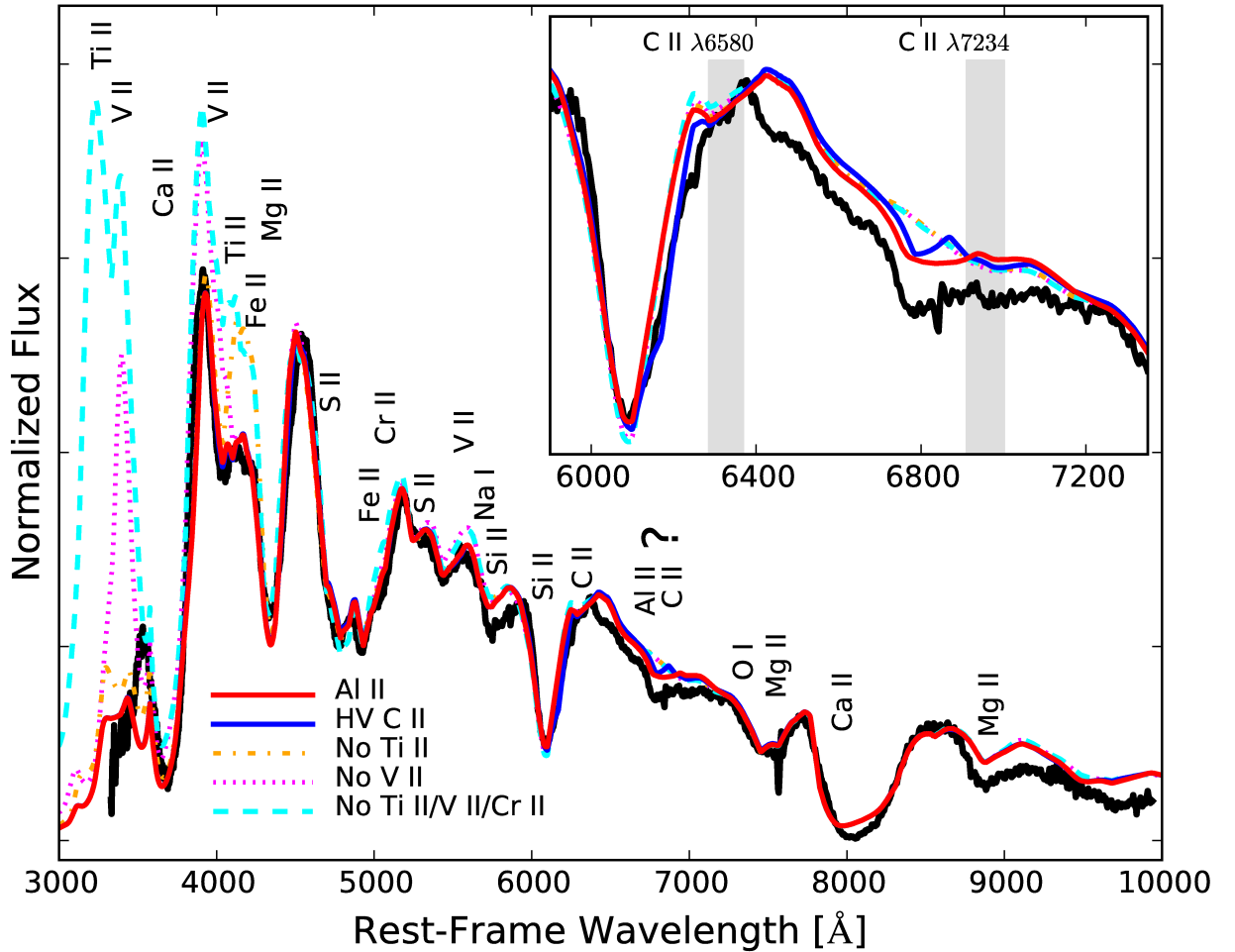


Figure 11. The -13 d spectrum of SN 2015F (black line) along with various `syn++` models (see Section 4 for details). The red line corresponds to a `syn++` model that includes photospheric Al II expanding at a velocity of 13000 km s^{-1} , and iron-peak elements (V II, Ti II, Cr II, and Fe II) expanding at a velocity of 14800 km s^{-1} . The blue line corresponds to a similar base model, but now includes a HV C II component expanding at a velocity of 20000 km s^{-1} , and not Al II. To show the contribution of iron-peak elements, we present the same base model but computed excluding Ti II (orange dot-dashed line), V II (magenta dotted line), and excluding Ti II, V II, and Cr II (cyan dashed line). In these models we do not include HV C II or Al II. The inset shows the region around the C II lines and the $\sim 6800 \text{ Å}$ feature. The grey regions mark the position of the photospheric C II lines moving at 10000 – 14000 km s^{-1} . The ions responsible for prominent spectral features are indicated on the figure. The spectrum of SN 2015F is corrected by Milky Way and host galaxy reddening.

and we show its expansion velocity in Fig. 9. The feature appears confined to a narrow range in velocity space from $\approx 18700 \text{ km s}^{-1}$ to $\approx 17000 \text{ km s}^{-1}$, but is persistent, and is still present in the spectrum at $+2$ d. The feature is also observed in SN 2007af at slightly higher velocities until -4 d, and then disappears.

The possibility that the HV features of C II and Ca II are produced close in velocity space may suggest a common origin for the HV material (see Fig. 9). HV Ca II features exhibit a plateau in their velocity evolution between -10 and -4 d (Fig. 9). At the same phase, the velocity measured for the possible HV C II $\lambda 7234$ feature is similar, but slightly lower.

5.3 Iron-group elements in SN 2015F

Using `syn++` to model the spectra of SN 2015F (see Section 4), we have identified lines of Ti II, V II, Cr II, and Fe II expanding at $\approx 14800 \text{ km s}^{-1}$. This implies a non-negligible amount of iron-group elements in the region between 15000 to 20000 km s^{-1} of the SN ejecta. Hatano et al. (1999) reported strong Fe II absorptions in the -12 d spectrum of SN 1994D at ~ 4300 and $\sim 4700 \text{ Å}$, and included in their `synow` model a HV Fe II component extending from 22000 km s^{-1} to 29000 km s^{-1} , to reproduce these features.

Strong and broad lines of iron-peak elements at such high-expansion velocities are generally unexpected in SNe Ia, since the pre-expansion suffered by the layers at higher velocities than 10000 to 13000 km s^{-1} will decrease the density too much to burn the material to iron-peak elements. Only in the case of a rapid tran-

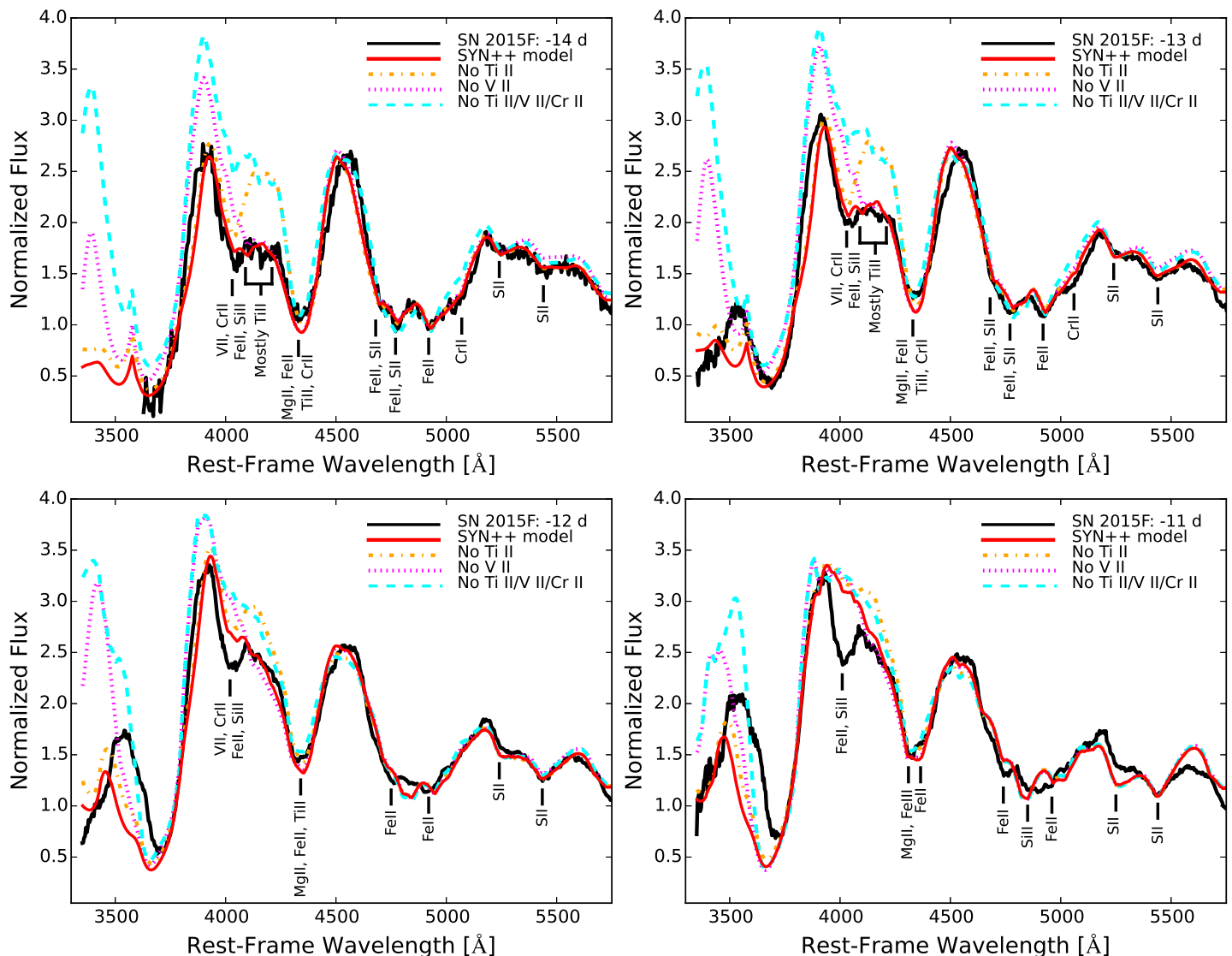


Figure 12. Early time spectra of SN 2015F (black line) along with various `syn++` models (see Section 4 for details). The red line corresponds to our best `syn++` model that includes iron-peak elements (V II, Ti II, Cr II and Fe II). To show the contribution of iron-peak elements, we present the same base model but computed excluding Ti II (orange dot-dashed line), V II (magenta dotted line), and Ti II, V II, and Cr II (cyan dashed line). In these models we do not include HV Cu or Al II. The ions responsible for prominent spectral features are indicated on the figure.

sition in the burning speed front, from a sub-sonic deflagration to a super-sonic detonation, would the flame burn the outermost layers ($v_{\text{exp}} > 13000 \text{ km s}^{-1}$) to iron-peak elements, yielding mainly radioactive ^{56}Ni and not enough IMEs to reproduce the characteristic spectral features of normal SNe Ia. The decay of ^{56}Ni mixed in the outermost layers can then heat the ejecta, producing strong lines of doubly-ionized species such as Fe III and Si III as in the brightest SNe. In the earliest spectra of SN 2015F ($< -12 \text{ d}$), this is not observed; by contrast, SN 2015F exhibits a spectrum dominated mainly by singly-ionized species (Fe II, Si II, S II, Ca II), consistent with a normal or relatively low ejecta temperature. At later phases, from about -11 d , SN 2015F begins to exhibit Si III $\lambda 4560$ and Si III $\lambda 5540$ lines, now suggesting heating from the decay of radioactive material mixed in the outer layers of the SN ejecta.

The absorption features produced by iron-group elements in the very early spectra of SNe Ia could be explained by iron-peak

elements synthesized during the SN explosion and mixed to the outermost layers of the SN ejecta, or as absorptions of iron-peak elements present in the white dwarf surface at the moment of the explosion (see [Lentz et al. 2000](#)) – or a combination of both. Recent three-dimensional delayed detonation models predict that freshly synthesized iron-peak elements are located mainly at intermediate velocities (~ 3000 to 10000 km s^{-1} ; [Seitenzahl et al. 2013](#)), the latter not corresponding with the observations of SN 2015F. However, [Seitenzahl et al. \(2013\)](#) remark that models with a strong (turbulent) deflagration phase, which are rather symmetric under rotation on large scales, exhibit strong inhomogeneities in the burning products on small scales. This may explain pockets of iron-peak material, observed at high-velocity, mixed in the outermost layers as in the case of SN 2015F.

To disentangle the metallicity of the progenitor from the fraction of freshly synthesized iron-group elements mixed to the

outermost layers would require a detailed modelling using the abundance tomography technique (Stehle et al. 2005; Mazzali et al. 2005; Tanaka et al. 2011; Hachinger et al. 2013; Mazzali et al. 2014). This is beyond the scope of this paper, and will be the subject of a future article.

6 SUMMARY

We have presented spectroscopic and photometric data for the nearby type Ia supernova SN 2015F, obtained as part of PESSTO. In particular,

(i) We show that SN 2015F is a normal, low-velocity gradient (LVG) SN Ia. The values of the parameters $\mathcal{R}(\text{Si II})$ (Section 3.1) and R_{HVF} (Section 3.3.2) are consistent with its decline rate ($\Delta m_{15}(B) = 1.35 \pm 0.03$).

(ii) We find moderate host galaxy reddening of $E(B - V)_{\text{host}} = 0.085 \pm 0.019$ mag. Assuming $H_0 = 70 \pm 3.0$ km s⁻¹ Mpc⁻¹, and the decline rate/peak luminosity calibrations of Phillips et al. (1999) and Kattner et al. (2012), we estimate $\mu_{\text{optical}} = 31.64 \pm 0.14$, and $\mu_{\text{NIR}} = 31.68 \pm 0.11$.

(iii) We model the Ca II H&K and NIR triplet profiles to estimate the expansion velocity and pseudo equivalent-widths of the photospheric and high-velocity components. We find that the high-velocity Ca II reached an expansion velocity of ≈ 23000 km s⁻¹, decreasing to ≈ 16500 km s⁻¹ just after maximum brightness. The expansion velocity of the photospheric Ca II component ranges from ~ 14500 km s⁻¹ at -14 d to ~ 10300 km s⁻¹ at maximum light.

(iv) We identify photospheric C II material moving at ≈ 14000 km s⁻¹ at the earliest epochs, which remains detectable until -4 d at an expansion velocity of ≈ 11000 km s⁻¹.

(v) We identify a broad absorption feature at ~ 6800 Å, previously unremarked upon in normal SNe Ia. We offer two possible explanations for this feature (Section 4): our favoured scenario is that it is produced by photospheric Al II $\lambda 7054$ expanding at 13000 – 11000 km s⁻¹. An overabundance of Al II relative to other SNe could be the result of a relatively high metallicity of the progenitor (Section 5.1). An alternative scenario is that it is produced by high-velocity (HV) C II $\lambda 7234$ expanding at 20000 – 18000 km s⁻¹ (see Section 5.2). The ~ 6800 Å feature is also common in SN 1991bg-like SNe.

(vi) We use syn++, to model the spectra of SN 2015F. We find lines of Fe-peak elements such as Ti II, V II, Cr II, and Fe II expanding at high velocity (> 14800 km s⁻¹) in the outermost layers of the SN. The inclusion of V II improves significantly our syn++ models at early times (-14 d and -13 d).

ACKNOWLEDGMENTS

We thank to the anonymous referee for his careful review that helped to improve this manuscript. We acknowledge support from STFC grant ST/L000679/1 and EU/FP7-ERC grant No. [615929]. Support for G.P. is provided by the Ministry of Economy, Development, and Tourism's Millennium Science Initiative through grant IC120009, awarded to The Millennium Institute of Astrophysics, MAS. K.M. acknowledges support from the STFC through an Ernest Rutherford Fellowship. A.G.-Y. is supported by the EU/FP7 via ERC grant No. [307260], the Quantum Universe I-Core program by the Israeli Committee for Planning and Budgeting and the ISF; by Minerva and ISF grants; by the Weizmann-UK "making connections" program; and by Kimmel and YeS awards. S.J.S.

acknowledges funding from ERC Grant agreement No. [291222] and STFC grants ST/I001123/1 and ST/L000709/1. This material is based upon work supported by the National Science Foundation under Grant No. 1313484. We are grateful to Bruno Leibundgut and Masayuki Yamanaka for providing the spectra of SN 1990N and SN 2012ht, respectively. This work is based on observations collected at the European Organisation for Astronomical Research in the Southern Hemisphere, Chile as part of PESSTO, (the Public ESO Spectroscopic Survey for Transient Objects Survey) ESO programme 191.D-0935, and on observations obtained with the Southern African Large Telescope (SALT) under program 2014-2-SCI-070.

REFERENCES

- Baltay C., et al., 2013, *PASP*, **125**, 683
 Benetti S., et al., 2004, *MNRAS*, **348**, 261
 Benetti S., et al., 2005, *ApJ*, **623**, 1011
 Bertin E., 2006, in Gabriel C., Arviset C., Ponz D., Enrique S., eds, *Astronomical Society of the Pacific Conference Series Vol. 351, Astronomical Data Analysis Software and Systems XV*.
 Bertin E., Mellier Y., Radovich M., Missonnier G., Didelon P., Morin B., 2002, in Bohlender D. A., Durand D., Handley T. H., eds, *Astronomical Society of the Pacific Conference Series Vol. 281, Astronomical Data Analysis Software and Systems XI*. p. 228
 Bianco F. B., et al., 2011, *ApJ*, **741**, 20
 Bildsten L., Shen K. J., Weinberg N. N., Nelemans G., 2007, *ApJ*, **662**, L95
 Blondin S., et al., 2012, *AJ*, **143**, 126
 Blondin S., Dessart L., Hillier D. J., Khokhlov A. M., 2013, *MNRAS*, **429**, 2127
 Bloom J. S., et al., 2012, *ApJ*, **744**, L17
 Bongard S., Baron E., Smadja G., Branch D., Hauschildt P. H., 2006, *ApJ*, **647**, 513
 Branch D., et al., 2003, *AJ*, **126**, 1489
 Brown P. J., et al., 2012, *ApJ*, **753**, 22
 Cao Y., et al., 2015, *Nature*, **521**, 328
 Cardelli J. A., Clayton G. C., Mathis J. S., 1989, *ApJ*, **345**, 245
 Cartier R., et al., 2014, *ApJ*, **789**, 89
 Cartier R., et al., 2015, *ApJ*, **810**, 164
 Childress M. J., et al., 2013, *ApJ*, **770**, 29
 Childress M. J., Vogt F. P. A., Nielsen J., Sharp R. G., 2014a, *Ap&SS*, **349**, 617
 Childress M. J., Filippenko A. V., Ganeshalingam M., Schmidt B. P., 2014b, *MNRAS*, **437**, 338
 Conley A., et al., 2008, *ApJ*, **681**, 482
 Crawford S. M., et al., 2010, in *Observatory Operations: Strategies, Processes, and Systems III*. p. 73725, doi:10.1117/12.857000
 Dopita M., et al., 2010, *Ap&SS*, **327**, 245
 Doull B. A., Baron E., 2011, *PASP*, **123**, 765
 Filippenko A. V., et al., 1992, *AJ*, **104**, 1543
 Firth R. E., et al., 2015, *MNRAS*, **446**, 3895
 Fisher A. K., 2000, PhD thesis, THE UNIVERSITY OF OKLAHOMA
 Fisher A., Branch D., Nugent P., Baron E., 1997, *ApJ*, **481**, L89
 Folatelli G., et al., 2010, *AJ*, **139**, 120
 Folatelli G., et al., 2012, *ApJ*, **745**, 74
 Folatelli G., et al., 2013, *ApJ*, **773**, 53
 Foley R. J., 2013, *MNRAS*, **435**, 273
 Foley R. J., et al., 2012, *ApJ*, **744**, 38
 Fraser M., et al., 2015, *The Astronomer's Telegram*, **7209**, 1
 Garavini G., et al., 2004, *AJ*, **128**, 387
 Garnavich P. M., et al., 2004, *ApJ*, **613**, 1120
 Gerardy C. L., et al., 2004, *ApJ*, **607**, 391
 Goobar A., et al., 2014, *ApJ*, **784**, L12
 Goobar A., et al., 2015, *ApJ*, **799**, 106
 Hachinger S., Mazzali P. A., Tanaka M., Hillebrandt W., Benetti S., 2008, *MNRAS*, **389**, 1087

- Hachinger S., Mazzali P. A., Taubenberger S., Pakmor R., Hillebrandt W., 2009, *MNRAS*, **399**, 1238
- Hachinger S., et al., 2013, *MNRAS*, **429**, 2228
- Hatano K., Branch D., Fisher A., Baron E., Filippenko A. V., 1999, *ApJ*, **525**, 881
- Hayden B. T., et al., 2010, *ApJ*, **722**, 1691
- Höflich P., Wheeler J. C., Thielemann F. K., 1998, *ApJ*, **495**, 617
- Höflich P., Gerardy C. L., Fesen R. A., Sakai S., 2002, *ApJ*, **568**, 791
- Hsiao E. Y., et al., 2013, *ApJ*, **766**, 72
- Hsiao E. Y., et al., 2015, *A&A*, **578**, A9
- Im M., Choi C., Yoon S.-C., Kim J.-W., Ehgamberdiev S. A., Monard L. A. G., Sung H.-I., 2015, *ApJS*, **221**, 22
- Iwamoto K., Brachwitz F., Nomoto K., Kishimoto N., Umeda H., Hix W. R., Thielemann F.-K., 1999, *ApJS*, **125**, 439
- Jennett T., Economou F., 2015, *Astronomy and Computing*, **9**, 40
- Jha S., Riess A. G., Kirshner R. P., 2007, *ApJ*, **659**, 122
- Kasen D., 2010, *ApJ*, **708**, 1025
- Kasliwal M. M., et al., 2010, *ApJ*, **723**, L98
- Kattner S., et al., 2012, *PASP*, **124**, 114
- Kessler R., et al., 2009, *PASP*, **121**, 1028
- Kobulnicky H. A., Nordsieck K. H., Burgh E. B., Smith M. P., Percival J. W., Williams T. B., O'Donoghue D., 2003, in Iye M., Moorwood A. F. M., eds, *Proc. SPIE Vol. 4841, Instrument Design and Performance for Optical/Infrared Ground-based Telescopes*. pp 1634–1644, doi:10.1117/12.460315
- Kriszunas K., et al., 2004, *AJ*, **127**, 1664
- Landolt A. U., 1992, *AJ*, **104**, 340
- Law N. M., et al., 2009, *PASP*, **121**, 1395
- Leibundgut B., Kirshner R. P., Filippenko A. V., Shields J. C., Foltz C. B., Phillips M. M., Sonneborn G., 1991, *ApJ*, **371**, L23
- Lentz E. J., Baron E., Branch D., Hauschildt P. H., Nugent P. E., 2000, *ApJ*, **530**, 966
- Lira P., et al., 1998, *AJ*, **115**, 234
- Maguire K., et al., 2012, *MNRAS*, **426**, 2359
- Maguire K., et al., 2014, *MNRAS*, **444**, 3258
- Maoz D., Mannucci F., Nelemans G., 2014, *ARA&A*, **52**, 107
- Marion G. H., Höflich P., Wheeler J. C., Robinson E. L., Gerardy C. L., Vacca W. D., 2006, *ApJ*, **645**, 1392
- Marion G. H., Höflich P., Gerardy C. L., Vacca W. D., Wheeler J. C., Robinson E. L., 2009, *AJ*, **138**, 727
- Marion G. H., et al., 2013, *ApJ*, **777**, 40
- Marion G. H., et al., 2015, *ApJ*, **798**, 39
- Marion G. H., et al., 2016, *ApJ*, **820**, 92
- Mazzali P. A., 2001, *MNRAS*, **321**, 341
- Mazzali P. A., Lucy L. B., Danziger I. J., Gouffes C., Cappellaro E., Turatto M., 1993, *A&A*, **269**, 423
- Mazzali P. A., Chugai N., Turatto M., Lucy L. B., Danziger I. J., Cappellaro E., della Valle M., Benetti S., 1997, *MNRAS*, **284**, 151
- Mazzali P. A., et al., 2005, *ApJ*, **623**, L37
- Mazzali P. A., Sauer D. N., Pastorello A., Benetti S., Hillebrandt W., 2008, *MNRAS*, **386**, 1897
- Mazzali P. A., et al., 2014, *MNRAS*, **439**, 1959
- Monard B., 2015, *CBET*, 4081
- Nomoto K., Thielemann F.-K., Yokoi K., 1984, *ApJ*, **286**, 644
- Nugent P., Phillips M., Baron E., Branch D., Hauschildt P., 1995, *ApJ*, **455**, L147
- Nugent P. E., et al., 2011, *Nature*, **480**, 344
- Olling R. P., et al., 2015, *Nature*, **521**, 332
- Parrent J. T., et al., 2011, *ApJ*, **732**, 30
- Parrent J. T., et al., 2012, *ApJ*, **752**, L26
- Pastorello A., et al., 2007, *MNRAS*, **377**, 1531
- Pereira R., et al., 2013, *A&A*, **554**, A27
- Perlmutter S., et al., 1999, *ApJ*, **517**, 565
- Persson S. E., Murphy D. C., Krzeminski W., Roth M., Rieke M. J., 1998, *AJ*, **116**, 2475
- Phillips M. M., Lira P., Suntzeff N. B., Schommer R. A., Hamuy M., Maza J., 1999, *AJ*, **118**, 1766
- Pignata G., et al., 2008, *MNRAS*, **388**, 971
- Pignata G., et al., 2011, *ApJ*, **728**, 14
- Piro A. L., Chang P., Weinberg N. N., 2010, *ApJ*, **708**, 598
- Planck Collaboration et al., 2014, *A&A*, **571**, A16
- Rabinak I., Waxman E., 2011, *ApJ*, **728**, 63
- Rau A., et al., 2009, *PASP*, **121**, 1334
- Riess A. G., et al., 1998, *AJ*, **116**, 1009
- Riess A. G., et al., 1999, *AJ*, **118**, 2675
- Riess A. G., et al., 2016, preprint, (arXiv:1604.01424)
- Schlafly E. F., Finkbeiner D. P., 2011, *ApJ*, **737**, 103
- Seitzzahl I. R., et al., 2013, *MNRAS*, **429**, 1156
- Shappee B. J., et al., 2016, *ApJ*, **826**, 144
- Silverman J. M., Filippenko A. V., 2012, *MNRAS*, **425**, 1917
- Silverman J. M., Vinkó J., Marion G. H., Wheeler J. C., Barna B., Szalai T., Mulligan B. W., Filippenko A. V., 2015, *MNRAS*, **451**, 1973
- Smartt S. J., et al., 2015, *A&A*, **579**, A40
- Smith J. A., et al., 2002, *AJ*, **123**, 2121
- Stehle M., Mazzali P. A., Benetti S., Hillebrandt W., 2005, *MNRAS*, **360**, 1231
- Stetson P. B., 1987, *PASP*, **99**, 191
- Tanaka M., Mazzali P. A., Maeda K., Nomoto K., 2006, *ApJ*, **645**, 470
- Tanaka M., Mazzali P. A., Stanishev V., Maurer I., Kerzendorf W. E., Nomoto K., 2011, *MNRAS*, **410**, 1725
- Taubenberger S., et al., 2008, *MNRAS*, **385**, 75
- Thomas R. C., et al., 2007, *ApJ*, **654**, L53
- Thomas R. C., Nugent P. E., Meza J. C., 2011a, *PASP*, **123**, 237
- Thomas R. C., et al., 2011b, *ApJ*, **743**, 27
- Tully R. B., 1988, *Nearby galaxies catalog*
- Tully R. B., Rizzi L., Shaya E. J., Courtois H. M., Makarov D. I., Jacobs B. A., 2009, *AJ*, **138**, 323
- Walker E. S., Hachinger S., Mazzali P. A., Ellis R. S., Sullivan M., Gal Yam A., Howell D. A., 2012, *MNRAS*, **427**, 103
- Yamanaka M., et al., 2014, *ApJ*, **782**, L35
- Yaron O., Gal-Yam A., 2012, *PASP*, **124**, 668
- Zhao X., et al., 2015, *ApJS*, **220**, 20
- Zheng W., et al., 2013, *ApJ*, **778**, L15
- Zheng W., et al., 2014, *ApJ*, **783**, L24

APPENDIX A: PHOTOMETRIC SEQUENCE AND PHOTOMETRY OF SN 2015F

This paper has been typeset from a \LaTeX file prepared by the author.

Table A1. *UBVgri* photometric sequence around SN 2015F.

R.A.	Decl.	<i>U</i>	<i>B</i>	<i>V</i>	<i>g</i>	<i>r</i>	<i>i</i>
07 ^h 35 ^m 04 ^s .6	−69°28′07″.9	17.348(0.036)	17.086(0.021)	16.245(0.015)	16.624(0.015)	15.974(0.020)	15.648(0.016)
07 ^h 35 ^m 05 ^s .6	−69°32′42″.3	–	17.431(0.019)	16.119(0.015)	16.753(0.015)	15.627(0.034)	15.114(0.016)
07 ^h 35 ^m 13 ^s .0	−69°29′57″.6	14.986(0.015)	14.724(0.015)	13.894(0.015)	14.267(0.015)	13.648(0.022)	13.374(0.015)
07 ^h 35 ^m 13 ^s .7	−69°27′05″.3	16.902(0.026)	16.672(0.019)	15.851(0.015)	16.215(0.015)	15.615(0.028)	15.303(0.020)
07 ^h 35 ^m 15 ^s .3	−69°27′11″.5	17.793(0.051)	17.455(0.015)	16.631(0.015)	17.006(0.015)	16.366(0.027)	16.078(0.024)
07 ^h 35 ^m 23 ^s .1	−69°35′15″.9	–	17.067(0.015)	15.755(0.015)	16.393(0.015)	15.242(0.024)	14.747(0.015)
07 ^h 35 ^m 27 ^s .9	−69°31′08″.2	16.829(0.021)	16.515(0.015)	15.674(0.015)	16.053(0.015)	15.454(0.031)	15.175(0.015)
07 ^h 35 ^m 32 ^s .7	−69°34′20″.4	15.082(0.015)	14.980(0.015)	14.279(0.015)	14.597(0.015)	14.102(0.020)	13.857(0.015)
07 ^h 35 ^m 35 ^s .9	−69°29′47″.4	17.640(0.029)	16.823(0.015)	15.639(0.015)	16.174(0.015)	15.270(0.023)	14.850(0.017)
07 ^h 35 ^m 37 ^s .7	−69°27′52″.7	16.210(0.015)	15.976(0.015)	15.180(0.015)	15.538(0.015)	14.970(0.021)	14.701(0.015)
07 ^h 35 ^m 38 ^s .0	−69°33′47″.9	16.575(0.015)	16.471(0.015)	15.747(0.015)	16.077(0.015)	15.541(0.019)	15.266(0.015)
07 ^h 35 ^m 43 ^s .7	−69°27′02″.1	18.004(0.015)	17.852(0.029)	16.881(0.015)	17.297(0.015)	16.588(0.034)	16.255(0.015)
07 ^h 35 ^m 44 ^s .6	−69°36′21″.3	16.595(0.015)	16.279(0.015)	15.424(0.015)	15.821(0.015)	15.172(0.027)	14.851(0.015)
07 ^h 35 ^m 45 ^s .0	−69°34′39″.3	17.238(0.015)	17.140(0.015)	16.413(0.015)	16.745(0.015)	16.217(0.028)	15.951(0.025)
07 ^h 35 ^m 46 ^s .2	−69°25′14″.4	17.877(0.077)	17.590(0.035)	16.762(0.020)	17.136(0.015)	16.523(0.015)	16.239(0.019)
07 ^h 35 ^m 47 ^s .2	−69°30′55″.2	17.448(0.052)	17.146(0.015)	16.267(0.015)	16.645(0.015)	16.016(0.018)	15.726(0.019)
07 ^h 35 ^m 54 ^s .2	−69°24′18″.9	16.011(0.015)	15.529(0.021)	14.591(0.015)	15.008(0.017)	14.277(0.015)	13.949(0.015)
07 ^h 35 ^m 57 ^s .1	−69°27′11″.7	14.316(0.015)	14.239(0.028)	13.585(0.015)	13.879(0.015)	13.425(0.016)	13.206(0.019)
07 ^h 35 ^m 59 ^s .4	−69°25′06″.6	17.916(0.015)	17.695(0.040)	16.835(0.015)	17.203(0.015)	16.628(0.020)	16.325(0.018)
07 ^h 36 ^m 02 ^s .5	−69°32′52″.7	17.660(0.049)	17.506(0.024)	16.787(0.015)	17.099(0.016)	16.624(0.039)	16.378(0.033)
07 ^h 36 ^m 06 ^s .9	−69°28′51″.4	17.593(0.015)	17.080(0.020)	16.144(0.015)	16.571(0.015)	15.883(0.017)	15.584(0.018)
07 ^h 36 ^m 13 ^s .8	−69°24′51″.1	16.904(0.019)	16.735(0.015)	15.955(0.015)	16.296(0.015)	15.743(0.015)	15.471(0.021)
07 ^h 36 ^m 14 ^s .1	−69°26′42″.1	18.312(0.015)	17.814(0.028)	16.887(0.015)	17.300(0.017)	16.648(0.029)	16.342(0.022)
07 ^h 36 ^m 19 ^s .2	−69°35′28″.7	–	18.400(0.037)	16.915(0.015)	17.666(0.015)	16.306(0.023)	15.686(0.016)
07 ^h 36 ^m 23 ^s .3	−69°23′58″.4	16.278(0.032)	15.856(0.017)	14.960(0.015)	15.363(0.015)	14.690(0.017)	14.375(0.015)
07 ^h 36 ^m 24 ^s .7	−69°24′57″.5	17.479(0.024)	16.983(0.021)	15.925(0.015)	16.403(0.015)	15.604(0.019)	15.193(0.023)
07 ^h 36 ^m 26 ^s .3	−69°26′17″.4	15.398(0.015)	15.385(0.015)	14.775(0.015)	15.048(0.015)	14.633(0.015)	14.419(0.018)
07 ^h 36 ^m 28 ^s .8	−69°24′58″.2	17.419(0.023)	17.241(0.036)	16.424(0.015)	16.785(0.015)	16.188(0.015)	15.913(0.017)
07 ^h 36 ^m 31 ^s .2	−69°29′59″.1	17.047(0.025)	16.957(0.036)	16.264(0.015)	16.575(0.015)	16.092(0.019)	15.852(0.042)
07 ^h 36 ^m 36 ^s .5	−69°36′14″.8	–	17.323(0.015)	16.201(0.016)	16.724(0.015)	15.811(0.023)	15.419(0.018)
07 ^h 36 ^m 39 ^s .1	−69°30′44″.3	18.161(0.015)	16.895(0.033)	15.618(0.015)	16.222(0.015)	15.132(0.015)	14.713(0.019)
07 ^h 36 ^m 48 ^s .8	−69°26′04″.2	15.990(0.015)	15.914(0.016)	15.240(0.015)	15.545(0.015)	15.071(0.015)	14.840(0.021)
07 ^h 36 ^m 54 ^s .2	−69°30′21″.3	17.652(0.086)	16.943(0.043)	15.925(0.026)	16.445(0.093)	15.560(0.015)	15.223(0.049)
07 ^h 36 ^m 59 ^s .4	−69°36′03″.3	17.206(0.015)	16.744(0.015)	15.845(0.015)	16.252(0.015)	15.604(0.019)	15.338(0.015)
07 ^h 36 ^m 59 ^s .9	−69°30′31″.0	18.021(0.015)	17.383(0.015)	16.437(0.015)	16.889(0.050)	16.198(0.084)	15.859(0.071)
07 ^h 37 ^m 02 ^s .8	−69°32′36″.0	16.793(0.030)	16.079(0.015)	15.079(0.015)	15.535(0.015)	14.762(0.019)	14.447(0.015)
07 ^h 37 ^m 07 ^s .5	−69°33′46″.2	16.625(0.118)	16.431(0.015)	15.630(0.015)	15.988(0.015)	15.410(0.021)	15.151(0.015)
07 ^h 37 ^m 09 ^s .5	−69°26′08″.7	15.328(0.015)	15.283(0.015)	14.671(0.015)	14.944(0.015)	14.527(0.015)	14.310(0.018)
07 ^h 37 ^m 15 ^s .3	−69°26′47″.6	16.037(0.015)	15.940(0.018)	15.285(0.015)	15.582(0.015)	15.122(0.015)	14.901(0.022)
07 ^h 37 ^m 21 ^s .6	−69°26′51″.1	15.735(0.015)	15.556(0.015)	14.822(0.015)	15.149(0.015)	14.632(0.015)	14.390(0.021)
07 ^h 37 ^m 24 ^s .8	−69°30′31″.8	15.893(0.015)	15.755(0.015)	15.028(0.015)	15.363(0.015)	14.838(0.027)	14.571(0.019)
07 ^h 37 ^m 26 ^s .8	−69°27′13″.2	15.614(0.015)	15.280(0.015)	14.451(0.015)	14.820(0.015)	14.228(0.016)	13.965(0.021)
07 ^h 37 ^m 27 ^s .5	−69°33′13″.9	–	17.418(0.021)	16.330(0.015)	16.829(0.018)	15.947(0.018)	15.572(0.016)
07 ^h 37 ^m 29 ^s .8	−69°33′01″.1	18.177(0.015)	17.834(0.015)	16.905(0.015)	17.318(0.015)	16.632(0.018)	16.316(0.017)

Numbers in parenthesis correspond to 1 σ statistical uncertainties.

Table A2. Optical photometry of SN 2015F

Date UT	MJD	<i>U</i>	<i>B</i>	<i>V</i>	<i>g</i>	<i>r</i>	<i>i</i>	Tel.
2015-03-08	57089.07	—	—	>19.017	—	—	—	8
2015-03-08	57089.18	—	—	>18.709	—	—	—	8
2015-03-09	57090.12	—	—	18.055(0.101)	—	—	—	8
2015-03-10	57091.80	—	17.156(0.027)	16.520(0.010)	16.850(0.010)	16.419(0.010)	16.593(0.010)	2
2015-03-11	57092.00	—	—	16.456(0.010)	—	—	—	7
2015-03-11	57092.99	—	—	15.857(0.019)	—	—	—	7
2015-03-12	57093.81	—	15.818(0.010)	15.436(0.010)	15.646(0.010)	15.382(0.013)	15.469(0.021)	2
2015-03-12	57093.90	—	15.757(0.010)	15.403(0.010)	15.574(0.010)	15.330(0.010)	—	1
2015-03-13	57094.10	—	15.682(0.010)	15.312(0.010)	15.494(0.010)	15.250(0.010)	15.315(0.010)	6
2015-03-13	57094.18	—	—	15.310(0.019)	—	—	—	7
2015-03-13	57094.91	15.056(0.048)	—	—	—	—	—	1
2015-03-14	57095.18	—	—	14.929(0.021)	—	—	—	7
2015-03-14	57095.18	14.971(0.011)	15.184(0.010)	14.898(0.019)	15.048(0.010)	14.832(0.018)	—	6
2015-03-14	57095.52	14.816(0.019)	15.049(0.030)	14.801(0.010)	14.938(0.010)	14.713(0.010)	14.784(0.010)	4
2015-03-14	57095.78	14.708(0.013)	14.915(0.010)	14.702(0.010)	14.805(0.010)	14.620(0.010)	14.696(0.024)	1
2015-03-14	57095.81	14.714(0.010)	14.912(0.010)	14.687(0.010)	14.818(0.010)	14.626(0.010)	14.682(0.010)	2
2015-03-15	57096.85	14.336(0.010)	14.562(0.010)	14.387(0.014)	14.496(0.011)	14.315(0.010)	14.391(0.010)	2
2015-03-16	57097.95	13.968(0.014)	14.279(0.012)	14.134(0.023)	14.206(0.014)	14.055(0.012)	14.127(0.025)	1
2015-03-17	57098.79	13.865(0.010)	14.085(0.014)	—	14.037(0.010)	13.881(0.010)	13.966(0.031)	1
2015-03-17	57098.82	13.876(0.063)	14.077(0.010)	13.945(0.010)	14.040(0.010)	13.879(0.010)	13.979(0.010)	2
2015-03-18	57099.48	13.735(0.010)	14.022(0.011)	13.858(0.010)	13.960(0.010)	13.780(0.010)	13.865(0.010)	5
2015-03-19	57100.84	13.504(0.010)	13.749(0.010)	13.640(0.010)	13.706(0.010)	13.584(0.010)	13.711(0.010)	1
2015-03-20	57101.52	13.470(0.010)	13.757(0.010)	13.608(0.020)	13.702(0.010)	13.542(0.010)	13.672(0.019)	5
2015-03-21	57102.53	13.369(0.014)	—	—	—	—	—	4
2015-03-21	57102.77	13.368(0.014)	13.600(0.010)	13.461(0.010)	13.536(0.010)	13.426(0.010)	13.628(0.010)	3
2015-03-22	57103.07	13.329(0.010)	13.581(0.010)	13.433(0.010)	13.516(0.010)	13.407(0.010)	13.591(0.010)	6
2015-03-23	57104.85	13.275(0.010)	13.461(0.010)	13.335(0.010)	13.401(0.010)	13.317(0.010)	13.619(0.027)	1
2015-03-23	57104.87	13.241(0.073)	—	—	—	—	—	3
2015-03-24	57105.78	13.264(0.010)	13.444(0.010)	13.288(0.010)	13.389(0.010)	13.288(0.010)	13.638(0.010)	2
2015-03-24	57105.85	13.255(0.026)	13.457(0.010)	13.293(0.010)	13.373(0.010)	13.283(0.012)	13.625(0.012)	1
2015-03-25	57106.87	13.260(0.010)	13.438(0.010)	13.264(0.010)	13.347(0.010)	13.268(0.010)	13.673(0.023)	1
2015-03-25	57106.90	13.306(0.024)	13.486(0.033)	—	—	—	—	3
2015-03-26	57107.46	13.259(0.010)	13.493(0.010)	13.277(0.010)	13.381(0.010)	13.265(0.010)	13.691(0.010)	4
2015-03-27	57108.40	13.313(0.010)	13.507(0.011)	13.281(0.010)	13.385(0.010)	13.285(0.010)	13.737(0.010)	4
2015-03-27	57108.52	—	13.551(0.013)	13.300(0.010)	13.438(0.010)	13.297(0.010)	13.740(0.010)	5
2015-03-28	57109.74	—	13.533(0.010)	13.268(0.010)	13.399(0.010)	13.263(0.010)	13.745(0.030)	1
2015-03-28	57109.77	—	13.569(0.010)	13.295(0.010)	13.438(0.010)	13.292(0.010)	13.776(0.010)	2
2015-03-29	57110.78	—	13.604(0.010)	13.291(0.010)	13.457(0.010)	13.287(0.010)	13.782(0.010)	2
2015-03-30	57111.80	—	13.710(0.010)	13.321(0.010)	13.501(0.010)	13.325(0.011)	13.818(0.010)	3
2015-03-30	57111.81	13.588(0.031)	13.675(0.010)	13.307(0.033)	13.499(0.010)	13.323(0.033)	13.827(0.022)	2
2015-04-03	57115.74	14.016(0.049)	14.081(0.010)	13.502(0.010)	13.767(0.010)	13.585(0.021)	14.070(0.010)	2
2015-04-07	57119.46	14.616(0.010)	—	13.766(0.012)	14.092(0.010)	13.817(0.010)	14.197(0.015)	5
2015-04-08	57120.75	—	14.712(0.010)	13.825(0.010)	14.202(0.010)	13.843(0.010)	14.181(0.023)	1
2015-04-08	57120.80	—	14.738(0.016)	13.884(0.021)	14.321(0.214)	13.844(0.010)	14.159(0.028)	3
2015-04-08	57120.87	—	14.724(0.010)	13.835(0.010)	14.219(0.010)	13.857(0.010)	14.166(0.026)	2
2015-04-08	57120.98	—	14.778(0.010)	13.875(0.011)	14.258(0.014)	13.876(0.010)	14.163(0.010)	6
2015-04-10	57122.37	—	—	13.955(0.086)	14.280(0.082)	—	—	4
2015-04-11	57123.02	—	15.020(0.016)	13.994(0.010)	14.461(0.010)	13.931(0.010)	14.134(0.010)	6
2015-04-11	57123.38	15.047(0.047)	15.067(0.010)	14.010(0.010)	14.508(0.010)	13.947(0.010)	14.107(0.010)	5
2015-04-12	57124.42	—	15.164(0.012)	14.094(0.010)	14.611(0.010)	13.982(0.010)	14.125(0.018)	4
2015-04-13	57125.43	—	15.301(0.036)	14.156(0.010)	14.716(0.014)	14.023(0.010)	14.100(0.010)	5
2015-04-14	57126.74	—	15.418(0.010)	14.209(0.010)	14.827(0.010)	14.021(0.010)	14.118(0.021)	1
2015-04-14	57126.78	—	15.456(0.010)	14.239(0.010)	14.855(0.010)	14.052(0.010)	14.130(0.010)	2
2015-04-16	57128.38	—	15.594(0.010)	14.331(0.022)	14.967(0.027)	14.101(0.010)	14.110(0.013)	5
2015-04-16	57128.77	15.881(0.028)	15.654(0.010)	14.359(0.015)	15.026(0.010)	14.131(0.010)	14.162(0.010)	2
2015-04-17	57129.79	—	15.723(0.036)	14.410(0.021)	15.121(0.020)	14.163(0.020)	14.178(0.026)	2
2015-04-18	57130.80	—	15.813(0.032)	14.488(0.030)	15.202(0.019)	14.212(0.023)	14.183(0.024)	2
2015-04-19	57131.82	—	15.869(0.052)	14.518(0.038)	—	—	—	3
2015-04-19	57131.86	—	15.859(0.070)	14.538(0.039)	15.302(0.023)	14.265(0.016)	14.205(0.051)	2
2015-04-20	57132.01	—	15.904(0.027)	14.547(0.022)	15.298(0.019)	14.274(0.031)	14.175(0.026)	6
2015-04-20	57132.79	16.155(0.024)	15.997(0.010)	14.625(0.032)	15.483(0.161)	14.313(0.024)	—	3
2015-04-20	57132.84	16.131(0.080)	—	14.594(0.010)	15.354(0.010)	14.299(0.032)	—	2

Table A2 – *continued* Optical photometry of SN 2015F

Date UT	MJD	<i>U</i>	<i>B</i>	<i>V</i>	<i>g</i>	<i>r</i>	<i>i</i>	Tel.
2015-04-21	57133.05	16.120(0.045)	15.982(0.025)	14.622(0.010)	15.396(0.010)	14.334(0.010)	14.223(0.010)	6
2015-04-21	57133.76	–	16.000(0.026)	14.650(0.048)	15.444(0.024)	14.380(0.023)	–	2
2015-04-21	57133.79	–	16.004(0.010)	14.669(0.010)	15.453(0.010)	14.366(0.010)	–	3
2015-04-21	57133.97	–	16.027(0.033)	14.687(0.022)	15.459(0.026)	14.386(0.023)	14.267(0.030)	6
2015-04-22	57134.71	–	16.147(0.032)	14.764(0.024)	15.505(0.023)	14.452(0.027)	14.300(0.021)	3
2015-04-24	57136.11	16.312(0.036)	16.178(0.010)	14.854(0.015)	15.616(0.010)	14.549(0.010)	14.402(0.023)	6
2015-04-27	57139.42	16.398(0.010)	16.354(0.010)	15.057(0.010)	15.800(0.010)	14.824(0.010)	14.694(0.010)	4
2015-05-01	57143.71	–	–	15.315(0.055)	16.045(0.055)	–	–	2
2015-05-02	57144.81	16.668(0.094)	16.625(0.043)	15.319(0.020)	16.025(0.010)	15.111(0.010)	15.011(0.010)	3
2015-05-05	57147.41	–	16.519(0.047)	15.350(0.025)	16.049(0.027)	15.191(0.022)	15.091(0.027)	4
2015-05-08	57150.74	16.773(0.033)	16.644(0.021)	15.456(0.012)	16.130(0.010)	15.285(0.010)	15.229(0.026)	1
2015-05-09	57151.77	–	16.811(0.059)	15.508(0.022)	–	–	–	3
2015-05-09	57151.81	16.686(0.072)	16.695(0.023)	15.504(0.010)	16.164(0.010)	15.342(0.010)	15.281(0.013)	1
2015-05-10	57152.06	16.853(0.055)	16.722(0.017)	15.536(0.013)	16.209(0.010)	15.382(0.010)	15.321(0.020)	6
2015-05-10	57152.73	–	16.722(0.035)	15.530(0.019)	16.187(0.021)	15.399(0.021)	15.319(0.022)	2
2015-05-10	57152.79	–	16.745(0.020)	15.547(0.010)	16.189(0.010)	15.392(0.010)	–	3
2015-05-10	57152.96	–	16.765(0.036)	15.563(0.018)	16.211(0.020)	15.399(0.023)	15.337(0.022)	6
2015-05-14	57156.35	–	16.795(0.053)	15.614(0.029)	16.220(0.032)	15.463(0.026)	15.431(0.034)	5
2015-05-16	57158.74	–	16.829(0.010)	15.648(0.010)	16.293(0.010)	15.560(0.030)	–	3
2015-05-17	57159.37	16.945(0.019)	16.800(0.010)	15.690(0.010)	16.281(0.010)	15.583(0.011)	15.561(0.023)	5
2015-05-18	57160.34	–	16.823(0.051)	15.717(0.021)	16.276(0.025)	15.601(0.026)	15.579(0.030)	4
2015-05-22	57164.98	–	16.924(0.056)	15.837(0.031)	16.405(0.042)	15.811(0.050)	–	6
2015-05-23	57165.40	16.986(0.090)	16.923(0.023)	15.869(0.024)	16.391(0.015)	15.781(0.010)	15.781(0.026)	4
2015-05-27	57169.69	–	17.024(0.068)	15.991(0.028)	–	–	–	3
2015-05-27	57169.73	–	16.966(0.035)	15.962(0.025)	16.478(0.022)	15.943(0.025)	15.972(0.026)	2
2015-05-28	57170.76	–	16.919(0.010)	15.910(0.023)	16.495(0.026)	15.897(0.010)	–	1
2015-06-04	57177.34	–	17.072(0.055)	16.126(0.025)	16.596(0.027)	16.169(0.031)	16.209(0.030)	4
2015-06-05	57178.96	–	17.134(0.049)	16.214(0.022)	16.645(0.017)	16.242(0.015)	16.263(0.029)	6
2015-06-07	57180.95	–	17.153(0.049)	16.246(0.030)	16.690(0.025)	16.267(0.029)	16.371(0.041)	6
2015-06-08	57181.72	–	17.166(0.031)	16.276(0.010)	16.664(0.013)	16.311(0.026)	–	3
2015-06-09	57182.72	–	17.159(0.031)	16.255(0.026)	16.639(0.017)	16.328(0.014)	–	1
2015-06-10	57183.37	–	17.077(0.075)	16.248(0.016)	16.736(0.227)	16.369(0.030)	16.345(0.010)	5
2015-06-11	57184.95	–	17.145(0.054)	16.346(0.029)	16.717(0.024)	16.402(0.027)	16.469(0.040)	6
2015-06-17	57190.70	–	–	–	16.784(0.010)	16.598(0.058)	–	3

Numbers in parenthesis correspond to 1σ statistical uncertainties.

Telescopes: 1=1m LCOGT-10/SAAO; 2=1m LCOGT-12/SAAO; 3=1m LCOGT-13/SAAO; 4=1m LCOGT-03/SSO; 5=1m LCOGT-11/SSO; 6=1m LCOGT-05/CTIO; 7=EFOSC-NTT/La Silla; 8=PROMPTs/CTIO.

Table A3. *JHK_s* photometric sequence around SN 2015F.

R.A.	Decl.	<i>J</i>	<i>H</i>	<i>K_s</i>
07 ^h 35 ^m 47 ^s .2	−69°30′55″.2	14.633(0.006)	14.264(0.019)	14.123(0.034)
07 ^h 36 ^m 31 ^s .2	−69°29′59″.1	14.866(0.032)	14.547(0.030)	14.366(0.048)
07 ^h 36 ^m 39 ^s .1	−69°30′44″.3	13.358(0.017)	12.796(0.017)	12.629(0.019)

Numbers in parenthesis correspond to 1σ statistical uncertainties.

Table A4. *JHK_s* Photometry of SN 2015F.

Date UT	MJD	<i>J</i>	<i>H</i>	<i>K_s</i>
2015-03-12	57093.17	15.092(0.014)	14.981(0.036)	14.939(0.046)
2015-03-12	57094.00	14.771(0.017)	14.668(0.032)	14.601(0.065)
2015-03-14	57095.03	14.441(0.021)	14.431(0.024)	14.222(0.027)
2015-03-19	57100.03	13.409(0.023)	13.466(0.023)	13.364(0.027)
2015-03-21	57102.04	13.329(0.033)	13.637(0.028)	13.271(0.035)
2015-03-29	57110.12	13.631(0.013)	13.703(0.012)	13.416(0.057)
2015-04-10	57122.12	14.652(0.010)	13.519(0.010)	13.481(0.029)
2015-04-12	57124.06	14.643(0.010)	13.508(0.010)	13.512(0.016)
2015-04-17	57129.03	14.399(0.010)	13.449(0.027)	13.404(0.010)
2015-04-27	57139.98	14.598(0.010)	13.941(0.010)	14.037(0.025)

Numbers in parenthesis correspond to 1σ statistical uncertainties.